Petrogenesis of zoned and unzoned mafic pegmatites: An insight from the Palaeoproterozoic mafic-ultramafic Hamn intrusion, Northern Norway

Paul Heckmann, Sabina Strmić Palinkaš, Harald Hansen, Giada Iacono-Marziano, Kristijan Rajič, Mélanie Forien, Steffen G Bergh

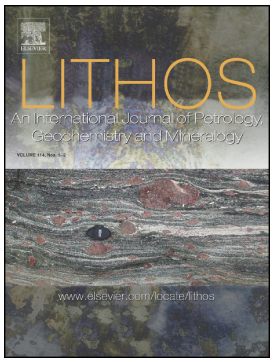

Petrogenesis of zoned and unzoned mafic pegmatites: An insight from the Palaeoproterozoic mafic-ultramafic Hamn intrusion, Northern Norway

Paul Heckmann, Sabina Strmić Palinkaš, Harald Hansen, Giada Iacono-Marziano, Kristijan Rajič, Mélanie Forien, Steffen G. Bergh

PII: S0024-4937(22)00227-4

DOI: https://doi.org/10.1016/j.lithos.2022.106818

Reference: LITHOS 106818

To appear in: *LITHOS*

Received date: 6 December 2021

Revised date: 25 July 2022

Accepted date: 30 July 2022

Please cite this article as: P. Heckmann, S.S. Palinkaš, H. Hansen, et al., Petrogenesis of zoned and unzoned mafic pegmatites: An insight from the Palaeoproterozoic mafic-ultramafic Hamn intrusion, Northern Norway, *LITHOS* (2022), https://doi.org/10.1016/j.lithos.2022.106818

Petrogenesis of zoned and unzoned mafic pegmatites: An insight from the Palaeoproterozoic mafic-ultramafic Hamn intrusion, Northern Norway

Paul Heckmann[1]*

Sabina Strmić Palinkaš[1,2]

Harald Hansen[1]

Giada Iacono-Marziano[1,3]

Kristijan Rajič[4]

Mélanie Forien[1]

Steffen G. Bergh[1]

[1]Department of Geosciences, UiT The Arctic University of Norway, Dramsvegen 201, 9037 Tromsø, Norway

[2]Department of Earth Science, University of Bergen, Allégaten 41, 5007 Bergen, Norway

[3]ISTO, UMR 7327 CNRS-Universite d'Orléans-BRGM, 1A rue de la Ferollerie, 45071 Orléans Cedex 2, France

[4]Université d'Orléans, ISTO, UMR 7327, 45071, Orléans, France

*Corresponding author. Telephone: +33 (0) 670595221. E-mail: paul.heckmann@uit.no

Keywords: mafic pegmatites; unzoned pegmatites; zoned pegmatites; undercooling; chlorine; CO_2

ABSTRACT

Mafic pegmatites have been reported from various geological environments, including ophiolites, layered magmatic intrusions, and volcanic arcs, but their petrogenesis stayed poorly constrained. This study brings new mineralogical and geochemical data obtained from unzoned and zoned gabbroic pegmatites hosted by the 1.8 Ga mafic-ultramafic Hamn intrusion, Northern Norway, with an aim to improve our understanding of the primary magmatic physicochemical factors that control the development of pegmatitic textures in mafic rocks.

The unzoned mafic pegmatites in the Hamn intrusion are hosted in gabbronorite and gabbro. The pegmatites differ macroscopically from the gabbronorite only by grain size and the color of feldspars. The bulk chemical compositions, including REE concentrations and rock-forming mineral assemblages of both rocks, are identical. The mineral composition of the pegmatite and host gabbro overlap. However, the pegmatite experienced epidotization and scapolitization, suggesting that H_2O- and chlorine were essential in the formation. Furthermore, the pyroxene of the pegmatite shows a more distinct negative Eu anomaly than the pyroxene of the host gabbronorite. Amphibole dyklets associated with the unzoned pegmatite pockets consist of Cl-rich pargasite and Cl-scapolite, indicating that the fluid pressure during crystallization of the unzoned pegmatites exceeded the confining pressure and resulted in the fracturing of host rocks and expulsion of a Cl- and H_2O-rich fluid and residual melt that subsequently formed amphibole veins.

The zoned pegmatites of the mafic-ultramafic Hamn intrusion are internally differentiated in terms of grain size, texture, and mineral composition. A characteristic comb-like diopside layering shows a change from numerous small to fewer larger grains from the rim towards the core of the pegmatite pocket. This textural change

suggests that the pegmatite-forming melt experienced a transition from a high nucleation rate (N) vs. growth rate (G) ratio to a low N/G ratio. A decreasing degree of undercooling with continuous crystallization from the rim to the core of the pockets can explain this transition. Apart from the comb-like layering, the bifurcating texture of some of the diopside grains is another evidence that the pegmatite-forming melt experienced undercooling. The pegmatites could have formed from a remobilized intercumulus or fractionated melt that was emplaced as residual melt into the colder host rock. Fast heat diffusion towards the host rock could have caused undercooling of the pegmatite-forming melt, which led to the formation of the comb-like and partly extremely coarse-grained texture. In contrast to the unzoned pegmatites, the zoned pegmatites lack evidence of significant involvement of chlorine- and H_2O. In contrast, the fluid inclusion study revealed that the pegmatite-forming melt was enriched in CO_2. Microthermometry of the CO_2-bearing inclusions indicates a minimum formation pressure of 647 to 734 MPa, and the titanium-in-quartz geothermometer yields a minimum formation temperature of 753 ± 34°C for the quartz segregation.

1. INTRODUCTION

Pegmatites are igneous rocks that either show grain sizes that are at least an order of magnitude larger than the largest crystals in the host rock (Beard and Scott, 2018), feature strongly directional growth habits, or both (London, 2008). Compositions of pegmatites can range from felsic to ultramafic (Beard and Scott, 2018; Cawthorn and Boerst, 2006; Strmić Palinkaš et al., 2012; Sunde et al., 2018), but granitic pegmatites, as an important source of industrial minerals (e.g., feldspars, quartz, micas, kaolinite; Glover et al., 2012), strategic metals (e.g., REE, Ta, Nb, Be, Sb, W, Li; Linnen et al., 2012) and gem-quality crystals of beryl, tourmaline, topaz, spodumene, and spessartine (e.g., Simmons et al., 2012) have attracted a dominant scientific attention over non-granitic types of pegmatites (London, 2008).

Since the pioneering work of Jahns and Burnham (1969), numerous studies have stressed the importance of fluxing components such as H_2O, B, F, P and Li (Bartels et al., 2013, 2011; London, 1984, Mahelek et al., 2010; Thomas et al., 2003), as well as CO_3^{2-} and HCO_3^- (Thomas and Davidson, 2012), for the formation of granitic pegmatites in particular. These fluxing components decrease the crystallization temperature, nucleation rates, melt polymerization, melt viscosity, and simultaneously increase diffusion rates (Fenn, 1977; Mysen and Richet, 2005; Shaw, 1963; Watson and Baker, 1991). On the other hand, experimental studies strongly support undercooling of the pegmatite-forming melt as the crucial condition responsible for the petrogenesis of felsic pegmatites (Devineau et al., 2020; London, 2014; Sirbescu et al., 2017). A melt is undercooled if it experiences a rapid cooling rate to a temperature below its liquidus, and the degree of undercooling is the temperature interval between the liquidus temperature and the crystallization temperature (Lofgren, 1974).

Mineral assemblages of mafic pegmatites are dominated by Ca-plagioclase, pyroxene, amphibole, olivine, and Fe-Ti oxide but can be enriched in hydrous minerals like amphibole and biotite, as well as quartz and apatite (e.g., Beard et al., 2002; Larsen and Brooks, 1994). Mafic pegmatites occur in a variety of geometric shapes, ranging from podiform bodies (pockets) to dikelets and semi-conformable sheets, and may show different geometries in the same locality (Cawthorn and Boerst, 2006; Larsen and Brooks, 1994; Péntek et al., 2006; Scoon and Mitchell, 2004; Viljoen and Scoon, 1985). Pegmatites may be classified as unzoned bodies that only differ in grain size to their host rock (Péntek et al., 2006) or zoned pegmatites that exhibit a modal zonation (Beard and Day, 1986; Lovering and Durrell, 1959; Péntek et al., 2006).

Several studies suggest that mafic pegmatites crystallize from volatile-rich residual melts gathered into pockets in crystal mush (Beard and Day, 1986; Beard and Scott, 2018; Larsen and Brooks, 1994; Lovering and Durrell, 1959; Péntek et al., 2006). For example, Péntek et al. (2006) proposed that unzoned and zoned pegmatites of the Szarvaskö Ophiolite complex in Northeast Hungary crystallized from a locally segregated hydrous melt, whose volatile and incompatible element content increased due to the local assimilation of adjacent sedimentary host rocks. In addition, deuteric alteration recorded by magnetite and pyroxene corrosion, accompanied by the formation of biotite and zoned amphiboles as well as plagioclase sericitization, support the evidence of the presence of a free aqueous phase during crystallization (Péntek et al., 2006). Larsen and Brooks (1994) suggest that the zoned pegmatites of the Skaergaard Intrusion in East Greenland formed from intercumulus liquids derived from the Skaergaard parental melt, based on the similarities in the composition of plagioclase and pyroxene with intercumulus products from the layered intrusion that host the pegmatites. Beard and Day (1986) also interpret the mafic pegmatites of the

Smartville complex in northern California as crystallized from intercumulus melt. In a further study, Beard and Scott (2018) suggest that H_2O saturation before the H_2O-buffering, incongruent crystallization of amphibole represents the critical factor for the formation of the Smartville pegmatites.

The present study aims to provide a better understanding about the role of chemical fluxes and undercooling on formation of unzoned and zoned mafic pegmatites. The study was conducted on mafic pegmatites hosted by the Paleoproterozoic mafic-ultramafic Hamn intrusion in Northern Norway and combines field observations, mineral chemistry, and lithogeochemical data from unzoned and zoned pegmatites and their associated host rocks, together with a fluid inclusion study of the zoned pegmatites.

2. REGIONAL GEOLOGICAL SETTING

2.1 West Troms Basement Complex

The Hamn gabbronorite (69°24'45.22 N, 17°09'01.89 E) is part of the Palaeoproterozoic mafic-ultramafic Hamn intrusion, located on the island of Senja in Troms and Finnmark County, Northern Norway (Fig. 1a). The island of Senja is a part of the West Troms Basement Complex, which is located along the Norwegian coastline from 69° to 70°N and to the west of the much younger (Paleozoic) Scandinavian Caledonian thrust nappes (Bergh et al., 2010). The West Troms Basement Complex is composed of Mesoarchean to Paleoproterozoic crust that is thought to be a part of the Fennoscandian Shield traced below the Caledonides (Bergh et al., 2015, 2010; Laurent et al., 2019; Myhre et al., 2013) (Fig. 1b). It evolved through multiple Archaean magmatic-orogenic events (2.72–2.62 Ga) followed by Palaeoproterozoic rifting/volcanism (2.5–2.0 Ga) and arc- and collisional orogenic

events at ca. 2.0–1.5 Ga, i.e., Svecofennian and Gothian orogens (Bergh et al., 2015, 2010; Myhre et al., 2013). Based on zircon U–Pb-isotope and Lu–Hf-isotope data, three Archean lithotectonic segments exist: (i) The northeastern segment is made up of juvenile tonalite-trondhjemite-granodiorite rocks (TTG), formed between 2.92 and 2.83 Ga. (ii) A younger southwestern segment is made of sanukitoid-like (quartz-) diorite-granodiorite-granite formed between 2.71–2.69 Ga, and (iii) there is an intervening reworked or micro-segment of 2.74–2.69 Ga sanukitoids and granites with minor 2.96 remnants (Laurent et al., 2019). Two major NW–SE trending terrain-boundary shear zone systems, the Kvalsund Shear Zone and the Senja Shear Belt, bound the lithotectonic segments (Fig. 1a). The Archean crust is overlain by several rift-related meta-volcanosedimentary sequences aged at 2.7 Ga to 1.9 Ga (Myhre et al., 2013) and intruded by mafic dyke swarms (2.4 and 2.2 Ga; Bergh et al., 2007, 2022; Kullerud et al., 2006).

In the late Palaeoproterozoic, a major plutonic suite of ca. 1.87–1.63 Ga quartz-monzonites, monzodiorites, and monzo-/syenogranite and dioritic mafic plutons intruded into the West Troms Basement Complex, e.g., the 1.8 Ga Ersfjord and Senja syenogranite pegmatites, and the similar aged Hamn gabbronorite (Bergh et al., 2010; Laurent et al., 2019), synchronous with the formation of the anorthosite-mangerite-charnockite-granite (AMCG) suite in Lofoten and Vesterålen (Fig. 1a; Corfu, 2007, 2004). In previous works, these magmatic rocks are considered to have formed as single magma batches by melting and fractional crystallization of mafic–intermediate lower crust or upper mantle rocks (Laurent et al., 2019). They are all part of the Transscandinavian Igneous Belt, a major plutonic episode that took place across the entire Fennoscandian shield (Högdahl et al., 2004). Shortly following this intrusion, a major orogenic event, i.e., the late-Svecofennian–early-Gothian orogen (<1.80–1.754

Ga), affected the entire West Troms Basement Complex (Armitage and Bergh, 2005; Bergh et al., 2015). The orogenesis led to NE–SW accretionary contraction, thrusting, and formation of a main metamorphic foliation at amphibole facies conditions. Upright macro-folding and later partitioned transpression with steep lateral ductile shear zones at greenschist facies conditions followed due to crustal uplift (Bergh et al., 2015). These events all influenced the present architecture of the Hamn gabbronorite (Fig. 2) and the surrounding gneisses in Senja.

2.2 The mafic–ultramafic Hamn intrusion

The mafic–ultramafic Hamn intrusion is located at the shoreline in the central part of Senja (Fig. 1a). It consists of two well-exposed, lens-shaped, and foliation-parallel bodies that are assumed to be connected beneath the surrounding TTG-gneisses (Fig. 2a). The age of the intrusion is 1800 ± 3 Ma, based on U–Pb dating of zircon (Corfu, 2013). The main body is predominantly composed of massive, medium-grained, homogeneous (apart from pegmatitic lenses) gabbronorite with well-preserved magmatic layering, striking 305–320° and dipping 50–80° NE. Lenses of peridotitic–pyroxenitic composition that seem to be conformable to the layering of the main gabbronorite have been found in the central portion of the intrusion (Fig. 2a). An increasing amount of plagioclase in the gabbronorite towards the NE indicates that the NE portion may represent the stratigraphically upper part of the intrusion. Despite the tectono-metamorphic overprint due to the late-Svecofennian–early-Gothian orogeny, the magmatic fabrics of the competent Hamn gabbronorite are remarkably well preserved, even close to the unit margins (Hansen et al., 2019). The western side of the unit, along its contact with the surrounding TTG-gneisses, is marked by a major thrust fault. However, the boundaries between the mafic and ultramafic lithologies are undeformed and mostly magmatic/intrusive with a marginal series of fine-grained

magnetite-bearing metagabbro. The eastern boundary is also thrust-related, and consists of partly mylonized rocks where the intrusion has been cut off against the Svanfjellet metasupracrustal belt, which represents the southeastern part of the Senja Shear Belt (Fig 1a) (Armitage, 2004; Henderson and Kendrick, 2003; Zwaan and Fareth, 2005).

3. SAMPLES AND METHODS

3.1 Sampling

Two types of pegmatites were sampled from the mafic–ultramafic Hamn intrusion. One type is texturally and mineralogically unzoned and therefore referred to as “unzoned pegmatite”. Nine samples of this pegmatite type, including their host rocks, were sampled along a road cut at the hotel 'Hamn I Senja' (Fig. 2b). The sample PH-HM-32 represents the transition from a fine-grained gabbro to a gabbronorite pegmatite (Fig. 3).

The other type of pegmatite is texturally and mineralogically zoned and therefore referred to as “zoned pegmatite”. Thirteen samples of the zoned pegmatites were collected, including three samples of the adjacent host rocks, two of which represent the overlying (Biotite metagabbro, PH-HM-25) and the underlying rocks (Biotite norite, PH-HM-26) of the largest pegmatitic body (Fig. 2c).

3.2 Analytical methods

The textural features were studied by transmitted and reflected polarized light microscopy. Identification of mineral phases and determination of their chemical compositions were performed using a Zeiss Merlin Compact VP field emission Scanning Electron Microscope, equipped with an Energy-dispersive X-Ray spectrometer from Oxford instruments at UiT The Arctic University of Norway and a Zeiss Merlin Compact FEG-SEM at the Institut des Sciences de la Terre d'Orléans (ISTO) in France. All Energy-dispersive X-Ray measurements were performed with a working distance of 8.5 mm, an accelerating voltage of 20 kV, and an aperture of 60 µm. Data reduction was carried out with Aztec software by Oxford Instruments at UiT, and BRUKER Quantax Esprit 2.1 at ISTO.

Major element compositions of minerals were analyzed with a Cameca SX Five electron-probe micro-analyzer at ISTO, using 15 kV accelerating voltage, 10 nA beam current, 10 s counting time for all elements, and a focused beam. Additional analysis was performed using a CAMECA SX100 at the Department of Geosciences at the University of Oslo, Norway, operating at 15 kV, 15nA and counting time on peak of 10s. The standards and detection limits are listed in Table A.2.

The whole-rock chemistry of 15 samples (Table A.1) was analyzed on approximately 5 g aliquots of homogenized powder at Actlabs (Activation laboratories Ltd. Canada), using the lithium metaborate/tetraborate fusion Inductively-Coupled-Plasma (ICP) method (analytical code *4LITHO)* for major elements, and the fusion Mass-Spectrometry (MS) methods (analytical code *WRA4B2)* for trace elements. In the fusion-ICP method the samples were mixed with a flux of lithium metaborate and lithium tetraborate and fused in an induction furnace. Immediately after the mixing, the molten melt was poured into a solution of 5% nitric acid and mixed continuously until completely dissolved. Solutions were analyzed with an ICP calibrated with USGS (United States Geological Survey) and CANMET (Canada Centre for Mineral and Energy Technology) certified reference materials. In the fusion MS method samples were fused, diluted and analyzed by ICP-MS, using three blanks and five controls each 40 samples.

The trace element composition of mineral grain separates of pyroxene and plagioclase were analyzed using the fusion MS method (analytical code *WRA4B2)* at Actlabs. Only pristine grains without other phases attached were collected by handpicking and pulverized in an agate mortar. The detection limits of the bulk geochemistry are listed in Table A.3.

Petrography and microthermometric measurements of fluid inclusions were performed on 100 to 300 μm thick double polished mineral wafers using a Linkam THM 600 stage, mounted on an Olympus BX 2 polarizing microscope equipped with 50x LWD objectives at UiT The Arctic University of Norway. Two synthetic fluid inclusion standards (SYNFLINC; pure H_2O and mixed H_2O - CO_2) were used for the calibration. The precision of the system was ± 0.2 °C in the temperature range between – 60 °C and + 10 °C. A JobinYvon LabRAM HR800 confocal Raman spectrometer equipped with a frequency-doubled Nd-YAG laser (100 mW, 532 nm) and a LMPlan FI 100× objective (Olympus) was used at the Department of Earth Science, University of Bergen, Norway, for the gas phase identification in the fluid inclusions at room temperature (ca. 20 °C).

The Ti concentration in quartz was measured using the Laser Ablation-ICP-MS at the Department of Geosciences Fluids Research Laboratory at Virginia Tech. The system features a GeolasPro Excimer 193 nm ArF laser ablation system coupled with an Agilent 7500ce quadrupole mass spectrometer. Samples were ablated in a 1.5 cm^3 ablation cell using a laser output energy of 150 mJ and adjusting beam diameter to ensure ablation of the entire unhomogenized melt inclusion. The ablation spot size was 24 μm with a dwell time of 10 milliseconds. A Ti concentration from transient signal profiles was determined by integrating signal intensities for all elements, correcting machine drift, and comparing intensity ratios with NIST glass standard SRM-610. The obtained data were reduced using the AMS software (Mutchler et al., 2008). The Si concentration in quartz was used as an internal standard and the detection limit of Ti was 5 ppm.

4. RESULTS

4.1 Field observations

The mafic-ultramafic Hamn intrusion hosts pockets of unzoned and zoned mafic pegmatites. Most of the unzoned pegmatite pockets are hosted in gabbronorite; however, the sample PH-HM-32 shows a sharp transition from a fine-grained host gabbro to a gabbronorite pegmatite. Due to its distinct transition, sample PH-HM-32 was used for the analysis of the mineral compositions between host gabbro and pegmatite. Although unzoned pegmatitic pockets have been observed in a variety of stratigraphic levels within the intrusion, the present study focuses on the unzoned pegmatites along a roadcut at the "Hotel I Senja" area (Fig. 2b). The unzoned pegmatites are <1 m in diameter and differ from their host rocks macroscopically only by the larger grain size and the lighter color of feldspar (Fig. 4a-c). The coarsening in grain size is usually abrupt, but pockets with a gradual coarsening towards the center of the pegmatite are also recorded (Fig. 4a, b). In addition, some of the unzoned pegmatite pockets show tail-like features filled with Cl-rich pargasite dikelets (Fig. 4c). Zoned pegmatites are less common, and so far only four zoned pockets (Fig. 5 and 6a) have been found at the tip of the shoreline at Hellandsnes in the northern part of the intrusion (Fig. 2b, for GPS data see Table A.1), close to the lenses of peridotitic–pyroxenitic composition in the central portion of the intrusion (Fig. 2b). The pockets occur end-to-end, spaced out ~10 m apart, and show an increase in size from NW to SE. The pockets are located in the same stratigraphic level, aligned parallel with the magmatic bedding, and are found in an area within the intrusion characterized by a narrow alternation of different mafic and ultramafic lithologies, visible in outcrops and drill cores. The smallest pocket in the NW is isometric in shape and has a diameter of ca. 80 cm (Fig. 5a). Two pockets further SE are elongated in shape with ca. 2-3 m in

the longest dimension (Fig. 5b) The largest pocket has the shape of a lens that is exposed about 10 m in length in the outcrop (Fig. 5c).

Most of the zoned pegmatites pockets consist of three modal zones (Fig. 5a, b): (i) a fringe zone (up to 10 cm thick) in contact with the host rock, (ii) a pegmatitic zone that shows either comb-like layered diopside (Pistone et al., 2016; Vernon, 1985; Zhang and Lee, 2020), or pegmatitic equigranular diopside, and (iii) a core zone. The largest pocket shows two additional features that are not present in the three smaller pockets: (i) A quartz segregation between the pegmatitic zone and the core zone and (ii) ~2 mm thick mafic dikelets in the core zone that radiate in all directions from a common center (Fig. 6b). The comb-like layering shows a characteristic change in the diopside grains from small and numerous to large and less numerous grains towards the center of the pockets (Fig. 6c, d).

4.2 Petrography and mineral compositions

4.2.1 Host gabbronorite

The gabbronorite consisting predominantly of plagioclase, orthopyroxene, hornblende, clinopyroxene and pargasite (Fig. 7a). Accessory minerals are biotite, scapolite, ilmenite, magnesio-hornblende, pyrite, pyrrhotite, chalcopyrite, chlorapatite, zircon, quartz, magnetite, and rutile. Plagioclase (An_{58-63}, n=10) has a mean size of ca. 2 mm and shows hypidiomorphic grains with polysynthetic twinning. Clinopyroxene ($En_{53-55}Fs_{17-18}Wo_{28-29}$, n=3) and orthopyroxene ($En_{69-74}Fs_{24-30}Wo_{0.3-5}$, n=11) grains are ca. 1.5 mm in size. Orthopyroxene is commonly rimmed by clinopyroxene (Fig. 7a). Plagioclase and pyroxene endmembers are shown in Fig 8. Hornblende (Cl content = 0.15 ± 0.09 wt%, n=15) replaces whole clinopyroxene grains, whereas pargasite (Cl content =0.84 ± 0.6 wt%, n=15) usually occurs along the grain boundaries of clino- and orthopyroxene. Biotite laths (Cl content = 0.31 ± 0.07 wt%, n=10) of up to 0.5 mm

are present within pargasite (Fig. 7b) and as an interstitial phase between plagioclase grains. Accessory chlorapatite (Cl content = 3.80 ± 0.13 wt%, n=5) is associated with pargasite or occurs as rare inclusions in plagioclase. The gabbronorite hosts pargasitic dikelets that are 5 to 15 mm in width. The pargasite (Cl = 0.78 ± 0.13 wt%, n=19) is surrounded by a fringe of numerous small grains of scapolite. Scapolite hosts needles of an aluminosilicate phase, 10-20 µm in size and chlorapatite inclusions (Cl content = 5.75 ± 0.69 wt%, n=12). The complete electron-probe micro-analyzer dataset is provided in the electronic appendix.

4.2.2 Host gabbro

The gabbro hosting sample PH-HM-32 (Fig. 3, T1, T2) differs in several aspects from the host gabbronorite of the other pockets: (1) the composition of plagioclase is more variable, with greater albitic components observed (An_{42-60}, in sample T1, n=33; An_{45-64}, in sample T2, n=26); (2) plagioclase grains contain <50 µm, needle-shaped epidote inclusions (Fig. 7d); (3) clinopyroxene compositions are more variable ($En_{48-60}Fs_{12-22}Wo_{28-38}$, in sample T1, n=29; $En_{42-55}Fs_{8-20}Wo_{28-50}$, in sample T2, n=14); (4) hornblende has a higher Cl content (Cl = 0.51 ± 0.16 wt%, in sample T1, n=4; Cl = 0.28 ± 0.08 wt%, in sample T2, n=3); (5) scapolite (Cl content = 1.78 ± 0.20 wt%, in sample T1, n=3) hosts epidote grains and fibrous aggregates of sillimanite (Fig. 7e); (6) chlorapatite (Cl content = 3.87 ± 0.77 wt%, in sample T2, n=7) is markedly more abundant; (7) orthopyroxene is absent; (8) ilmenite with magnetite exsolution lamellae is commonly observed surrounded by euhedral almandine garnet and small laths of biotite. The overgrowth of ilmenite by garnet at the contact between ilmenite and plagioclase, the euhedral morphology of almandine, and the small biotite grains surrounding ilmenite, suggest that almandine is not a primary magmatic phase but instead a recrystallization product.

4.2.3 Unzoned pegmatites

The pegmatite consisting predominantly of plagioclase, orthopyroxene, hornblende, clinopyroxene and pargasite (Fig. 7f). Plagioclase has a more albitic composition than in the gabbro (An_{30-57}, T4, n= 14 and An_{41-56}, in sample T5, n=19), and contains needle-shaped epidote inclusions (Fig. 7g). Similar to the gabbro, clinopyroxene ($En_{41-59}Fs_{11-21}Wo_{26-48}$, in sample T4, n=12; $En_{52-60}Fs_{14-19}Wo_{25-29}$, in sample T5, n=13) and orthopyroxene grains ($En_{67-71}Fs_{24-29}Wo_{1-5}$, in sample T4, n=5; $En_{70-74}Fs_{25-29}Wo_{1-5}$, is sample T5, n=5) show rims of pargasite (Cl content = 0.23 ± 0.13 wt%, in sample T4, n=9; Cl content = 1.48 ± 0.29 wt%, in sample T5, n=23) in contact with plagioclase (Fig. 7h). In one sample (KR-HM-24), orthopyroxene exhibits a sympletitic texture with Fe-Ti oxides (Fig. 7i). The pargasitic rim around pyroxenes also hosts sulfide assemblages composed of pyrite, pyrrhotite, chalcopyrite and pentlandite (Fig. 7j). Locally, scapolite (Cl = 0.99 ± 0.27 wt%, T4, n=5) occurs between the pargasitic rim and plagioclase, and hosts aggregates of pargasite. Almandine overgrowth of ilmenite is present at the grain boundary of plagioclase crystals (Fig. 7h) and within the pargasitic rim (Fig. 7k). Biotite and chlorapatite are spatially associated with pargasite (Fig. 7l).

4.2.4 Host rocks to the zoned pegmatites

The stratigraphically lower host rock is a Biotite norite characterized by presence of large biotite grains (PH-HM-26, Fig. 9a). The stratigraphically upper host rock is a Biotite metagabbro that has experienced deuteric alteration but not epidotization. It shows mostly numerous small biotite grains (Cl = 0.53 ± 0.04 wt%, n = 9) ca. 0.1 mm in lengths within scapolite (PH-HM-25, Fig. 9b).

4.2.5 Zoned pegmatite

The zoned pegmatites show a fine-grained fringe zone at the contact with the host rock that consists predominantly of fine-grained albitic plagioclase (An_{4-8}, n=9), scapolite and minor amounts of augitic clinopyroxene ($Wo_{25-38}En_{40-57}Fs_{18-32}$, n=12) surrounded by pargasite. Accessory phases are titanite and biotite (Fig. 9c).

The adjacent pegmatitic clinopyroxene zone is composed of diopside laths ($Wo_{47-48}En_{40-41}Fs_{12-13}$, n=5) up to 15 cm long, which in most parts feature a comb-like layering, but in some parts shows unoriented grains (Fig. 5e). The diopside shows single twinning (Fig. 9d) and mineral inclusions of albite and ilmenite. Albitic plagioclase (An_{5-8}, n=10) and Cl-scapolite are present in the matrix interstitial to the large diopside laths. The quartz segregation zone consists exclusively of quartz (Fig. 9e), which hosts exsolutions of rutile. The core zone consists primarily of plagioclase (An_{2-6}, n=9) and quartz (Fig. 9e, f) with minor amounts of amphibole. In contrast to the unzoned pegmatites, the plagioclase of the zoned pegmatites lacks epidotization.

4.3 Whole-rock compositions and trace element compositions of selected mineral phases

4.3.1 Unzoned pegmatites

The major element composition of the pegmatitic sample (KR-HM-36) resembles the composition of its associated host gabbronorite (KR-HM-28). The pegmatite has slightly lower SiO_2 and total Fe_2O_3 and is richer in MgO compared to the host gabbronorite (Table 1). Most trace elements are also present in similar concentrations in both rocks (Table 2). However, Cr, Ni, and Cu show higher concentrations in the pegmatite (80 versus 180 ppm Cr, 30 versus 70 ppm Ni, 20 versus 50 ppm Cu).

The primitive mantle-normalized (PRIMA) rare earth element (REE) pattern of the host gabbronorite and unzoned pegmatite (normalization values are pyrolite after McDonough and Sun, 1995) overlap and show a strongly fractionated light REE (LREE) segment ($2.41 < La_N/Sm_N < 2.54$), a less strongly fractionated heavy REE (HREE) segment ($1.59 < Gd_N/Lu_N < 1.90$) and a positive Eu anomaly ($1.64 < Eu_N/Eu_N^* < 1.99$) (Fig. 11a). The sum of the REE of the gabbronorite and pegmatite is 26.8 and 27.3 ppm, respectively.

Plagioclase and pyroxene separated from the unzoned pegmatite show enrichment in REE, especially HREE, compared to the host gabbronorite (Fig. 11b). Plagioclase shows a strongly fractionated LREE segment ($7.79 < La_N/Sm_N < 9.09$), a less strongly fractionated HREE segment ($2.71 < Gd_N/Lu_N < 4.22$) and a positive Eu anomaly ($5.92 < Eu_N/Eu^*_N < 6.48$) for both types of rocks. In contrast, pyroxene shows a flat LREE segment ($0.63 < La_N/Sm_N < 0.89$), a less strongly fractionated HREE segment ($1.61 < Gd_N/Lu_N < 1.84$) and a negative Eu anomaly ($0.78 < Eu_N/Eu_N^* < 0.93$) (Fig. 11b). The pyroxene of the pegmatite is richer in REE. It shows a more pronounced negative Eu anomaly than the host gabbronorite (Fig. 11b).

4.3.2 Zoned pegmatites

The major and trace element compositions of each zone of the largest zoned pegmatite pocket (Figs. 5c and 6a) are provided in Tables 1 and 2, respectively. A general enrichment in SiO_2 from the gabbronorite (~53 wt. % SiO2) to the center of the pegmatite (~72 wt. % SiO2) is observed (Table 1). The fringe zone is slightly enriched in SiO_2, Fe_2O_3, and Na_2O, and depleted in Al_2O_3, MgO, CaO, and K_2O compared to the host rocks. The major element composition of the pyroxene zone reflects the composition of the pegmatitic diopside, with the minor addition of plagioclase (Table 1). The core zone is enriched in SiO_2 and Na_2O compared to all

other zones. The general shape of the REE patterns show strongly fractionated LREE and less strongly fractionated HREE (Fig. 11c). The fringe zone features the highest sum of REEs (~ 218 ppm), whereas the core zone shows the lowest REE abundances (~ 54 ppm). The pegmatitic clinopyroxene zone exhibits a negative Eu anomaly (Eu_N/Eu_N^* = 0.67), which is not observed in the other zones (Fig. 11c) and suggests significant plagioclase fractionation before diopside crystallization.

The primitive mantle-normalized REE pattern of the plagioclase of the pegmatitic zone resembles those of the plagioclase of the unzoned pegmatite (Fig. 11d); however, the positive Eu anomaly of the former is less evolved (Eu_N/Eu_N^* = 1.52). On the other hand, clinopyroxene from the pegmatitic zone is more enriched in LREE and features a more negative Eu anomaly (Eu_N/Eu_N^* = 0.52) compared with clinopyroxene from the unzoned pegmatites (Fig. 11d), suggesting comparatively more abundant plagioclase fractionation prior to diopside crystallization in the zoned pegmatite.

4.4 Fluid inclusions studies

Quartz from the quartz segregation zone and pyroxene from the pegmatitic zone contain CO_2-rich fluid inclusions. The fluid inclusions occur in isolated clusters or are aligned along growth zones. The inclusions hosted by quartz have isometric to elongated shapes and range in size from <5 up to 20 μm. The pyroxene-hosted inclusions always have elongated shapes, and range in size from <5 up to 10 μm. At room temperature, the fluid inclusions hosted by both minerals apparently contain a single phase (Fig. 12a-c). Raman spectroscopy has revealed CO_2 as the main component of the fluid inclusions (Fig. 12d). In addition, a weak shoulder in the 3000 cm^{-1} wavenumber region indicates the presence of minor amounts of H_2O. Although the liquid aqueous phase has not been optically recorded, the Raman spectroscopy

data suggest that at room temperature a minor amount of liquid H_2O may occur as a thin film along fluid inclusion walls.

Microthermometric data have been obtained only from quartz-hosted fluid inclusions (Fig. 12), as the dark color of pyroxene prevents reliable microthermometric measurements. When cooled down to -120°C, the CO_2 inclusions froze to aggregates of solid CO_2. The melting temperature ($TmCO_2$) ranges from -60 to -57°C and has a mean of -57.6 ± 0.6°C (1s, n = 20 in 2 samples, Table A.4). The approximate 1°C deviation from the triple point of pure CO_2 (-56.6°C, Van Den Kerkhof and Thiéry, 2001) may reflect a contribution of an additional volatile such as methane, nitrogen and/or noble gasses, but their presence has not been recorded by Raman spectroscopy. On the other hand, the presence of H_2O does not significantly affect the CO_2 triple point (Diamond, 2001). The homogenization into liquid (L) phase ($ThCO_2$) has been recorded in the range between -33 and -21.9°C (mean value at -28.4 ± 3.2°C, 1s, n = 20 in 2 samples, Table A.4), corresponding to the CO_2 density between 1.04 and 1.09 g/cm^3 (Span and Wagner, 1996).

4.5 Thermobarometry

Quartz from the zoned pegmatites that host the CO_2 fluid inclusion also contains oriented needles of exsolved rutile (Fig. 12b). The titanium content in quartz, measured by LA-ICP-MS, is 102 ± 34 ppm (n=14, Table A.5). The titanium-in-quartz geothermometer by Wark and Watson (2006) indicates that quartz crystalized at 753 ± 34°C. The intersection of representative fluid inclusion isochores, constructed based on the equation of state by (Pitzer and Sterner, 1994) and using the Excel spreadsheet published by Hansteen and Klügel (2008), with the titanium-in-quartz geothermometer yield the formation pressure of

647 to 734 MPa.

5. DISCUSSION

5.1 Petrogenesis of the unzoned pegmatites

The unzoned pegmatites presented in this study share an almost identical bulk composition with the associated gabbronorite (Table 1). The mineral composition of the fine-grained host gabbro in sample PH-HM-32 (Fig. 3) overlaps with that of the pegmatite (Fig. 8). The host gabbro of this sample does not contain orthopyroxene; however, orthopyroxene is present of the host gabbronorite of other pegmatitic pockets. The occurrence of orthopyroxene in pegmatites and not in their host rocks has been reported in the Smartville Complex, and attributed to the crystallization of pegmatites from the intercumulus melt of the host cumulates (Beard and Day 1986). The major element (Table 1) and trace element (Table 2) compositions of the Hamn unzoned pegmatites do not show, however, any evidence for an intercumulus origin. The main differences between the unzoned pegmatite pockets and the gabbronorites are (i) the abundant epidotization and scapolitization of plagioclase (Fig. 6a, b vs. Fig 6c, d), and (ii) the occurrence of Cl-scapolite associated with plagioclase, chlorapatite and Cl-bearing pargasitic amphibole at the grain boundaries between pyroxene and plagioclase (Fig. 7g). Both epidotization and the texture of these Cl-bearing phases suggests deuteric alteration of the primary, early-formed magmatic phases.

The epidotization of plagioclase, in particular, indicates breakdown of plagioclase in the presence of a fluid phase at elevated temperatures (Goldsmith, 1982; Goldsmith and Chicago, 1982). Due to the absence of field evidence for deformation and externally derived fluids, we propose that the Cl-bearing hydrous fluid was derived from second boiling of the pegmatite-forming melt. During the waning stages of crystallization, the abundant formation of anhydrous phases might have led to the

enrichment of H_2O and Cl in the residual melt until their solubilities were reached resulting with the exsolution and infiltration of a H_2O and Cl-rich fluid phase.

Some of the unzoned Hamn pegmatite pockets show tail-like features filled with Cl-rich amphibole veins (Fig. 4c). These features additionally support the process of exsolution of a free fluid phase. Due to the volume increase, the fluid pressure might have exceeded the confining pressure causing hydrofracturing of the adjacent host rock even at ductile conditions (Brown, 2013). The expulsion of the residual melt and fluid into the formed fractures resulted in crystallization of the Cl-rich amphibole veins associated with fine-grained Cl-scapolite (Fig. 7c). The same mechanism was proposed by Vasyukova and Williams-Jones (2014) for the fracturing of pegmatites of the Strange Lake Pluton, Canada.

The presence of chlorapatite inclusions in pargasite within the pegmatite and associated host rock is additional evidence for the high activity of Cl during the formation of both rocks. In contrast to amphiboles and micas, the Cl content of apatite is not dictated by the crystal-chemical factors (Boudreau and Mccallum, 1989) and can act as a chlorimeter, indicating the late-stage magmatic conditions preserved in apatite when the rock becomes impermeable close to solidus temperatures (Mathez and Waight, 2003). However, it is not clear if the chlorapatite and the host pargasite formed at magmatic conditions or during metasomatism in the absence of melt. Nevertheless, the fact that the size of chlorapatite grains positively correlates with the size of the primary magmatic phases might speak in a favor of the magmatic origin of chlorapatite.

The exact role of H_2O and Cl in the formation of the unzoned pegmatites of the Hamn intrusion is still unclear, but elevated Cl contents in association with mafic pegmatites are not unique to the Hamn locality; for example it is reported by Meurer and Boudreau (1996) for the Stillwater igneous complex in Montana, USA; by Sonnenthal (1992) for

pegmatites from the Skaergaard intrusion; and by Péntek et al. (2006) for the pegmatites of the Szarvaskö Complex, Hungary. Sonnenthal (1992) reported that apatite, biotite, and amphibole in dendritic anorthosites and pegmatites from the Skaergaard intrusion have higher Cl contents than those found in the surrounding host rocks, and interpreted them to indicate the presence of high-temperature aqueous fluids having high HCl/HF fugacity ratios. Further, epidotization (saussuritization) of plagioclase has also been reported from pegmatites of the Smartville Complex in California (Beard and Scott, 2018).

Experimental studies (e.g., Fenn, 1977; Mysen and Richet, 2005; Shaw, 1963; Watson and Baker, 1991; Webb et al., 2014) suggest that H_2O and Cl may affect the rheology of mafic melts, reduce the viscosity of the melt and increase diffusion rates, which might decrease crystal nucleation rate (N) over growth rate (G), therefore favoring the growth of a few large crystals over the growth of numerous smaller crystals. We therefore suggest that locally higher H_2O and Cl contents in the silicate melt may be instrumental for the formation of the unzoned pegmatite pockets within the gabbronorites.

The origin of the H_2O and Cl has not been clearly determined, but we suggest it is magmatic. The accretionary geological setting of the mafic-ultramafic Hamn intrusion suggests it formed by melting of mafic–ultramafic lower crust or upper mantle rocks (Laurent et al., 2019), as part of an arc-related magmatic system (Bergh et al., 2022, 2010; Laurent et al., 2019). High volatile contents usually characterize such magmas (e.g., Zellmer et al., 2015).

5.2 Petrogenesis of the zoned pegmatites

The comb-like layering texture of the pegmatitic diopside (Fig. 6c, d) is the most prominent textural feature of the zoned pegmatite. Because of the asymmetry of the

comb-like layers, they are considered to be a variant of unidirectional solidification textures (e.g., Pistone et al., 2016). Comb-like layering textures and bifurcated diopside grains are commonly associated with undercooling of the rock-forming melt and reflect heterogeneous nucleation (Pistone et al., 2016; Simmons and Webber, 2008; Vernon, 1985; Zhang and Lee, 2020). The process responsible for undercooling may be thermal-, chemical- or pressure-controlled quenching (Pistone et al., 2016; Simmons, 2007; Simmons and Webber, 2008), or the exsolution of a volatile phase under adiabatic conditions (Mastin and Ghiorso, 2001).

The comb-like layering in the Hamn zoned pegmatites shows a change from numerous, small diopside grains to fewer and larger diopside grains towards the center of the zoned pockets (Fig. 13), likely reflecting a change in the degree of undercooling. A high degree of undercooling leads to a high nucleation rate/growth rate (N/G) ratio and the crystallization of numerous small grains, whereas a low degree of undercooling leads to a lower N/G ratio and the crystallization of fewer large grains (Fenn, 1977; Swanson, 1977). A decrease in the crystal number density and an increase in grain size from rim to the core is also reported for hornblende from orbicular granitoids, which is interpreted being formed by the rapid, disequilibrium crystallization of hot dioritic to tonalitic melts injected into a cooler granitic magma (Zhang and Lee 2020). On the other hand, due to the lack of graphic textures and the presence of high-temperature minerals, Beard and Scott (2018) disregard the role of undercooling in the formation of the mafic Smartville pegmatites. Graphic textures, however, are observed in experimental studies only for granitic compositions at high degrees of undercooling (Devineau et al., 2020). Therefore, a lack of these textures does not exclude lower or moderate degrees of undercooling, which would favor low N/G ratio, and therefore the formation of large grain sizes.

The higher albite content in plagioclase in all zones of the pegmatite compared to the host gabbronorite indicates that the pegmatite-forming melt was more evolved compared to the host rock-forming melt (Fig. 10a). The area around Hellandsnes is characterized by alternating mafic and ultramafic lithologies, pointing to a highly dynamic magma system, in which the disruption of the cumulate pile (e.g., Beard, 1986; Viljoen and Scoon, 1985) could have been an efficient mechanism for segregation of already fractionated intercumulus melt. The segregated melt could have been injected into the colder gabbronorites, generating the sharp transition and the diopside comb-like layer. Heat diffusion from the injected melt to the colder host gabbronorite may explain the undercooling features. The formation of mafic pegmatites in other intrusions worldwide has been chiefly ascribed to the crystallization of intercumulus melts. Many of those pegmatites are indeed zoned, having pyroxene-rich (Péntek et al., 2006) or plagioclase-rich rims (Beard and Day, 1986; Larsen and Brooks, 1994) and cores containing quartz (Larsen and Brooks, 1994; Péntek et al., 2006), similar to the zoned pegmatites of the Hamn intrusion.

The absence of hydrous minerals indicates that an aqueous fluid phase did not play a crucial role in formation of the zoned pegmatites. Moreover, epidotization and scapolitization of plagioclase, clear evidence for the presence of a fluid phase (Goldsmith, 1982), are observed in the zoned pegmatites, although this might be related to a high sodium composition of plagioclase and the lack of calcium to form epidote grains. The presence of CO_2-rich but H_2O-poor fluid inclusions in quartz and diopside additionally indicates a low H_2O activity. H_2O-poor, carbonic-rich fluid inclusions are not a unique feature of the Hamn intrusion pegmatites. They have also been found in quartz, apatite, and magnesio-hornblende from the mafic pegmatites of the North Roby Zone, Lac des Iles Complex, Ontario, Canada (Hanley and Gladney,

2011). The experimental study of Suzuki (2018) observed that CO_2 reduces the viscosity in a melt of jadeite composition at high pressures (> 2 GPa). By reducing the viscosity, CO_2 might inhibit nucleation and promote the growth of large crystals. More research on the effect of CO_2 on the viscosity of basaltic melt at lower pressures is however needed to understand the role of CO_2 on the formation of mafic pegmatites. The high CO_2 fugacity may reflect high CO_2 content of the magma, which contrasts with the high H_2O and Cl contents observed in zoned pegmatites. Alternatively, CO_2 might be related to the interaction of the pegmatite-forming magma with carbon-bearing supracrustal rocks. Furthermore, supracrustal xenoliths composed predominantly of plagioclase and quartz, and tonalitic gneisses from the underlying basement, were observed along the shoreline at Hellandsnes ca. 50 m southeast from the zoned pegmatites. The presence of xenoliths of tonalitic composition in the vicinity of the zoned pegmatites raises the question of a xenolithic origin for the zoned pegmatites. Xenoliths of tonalitic host rocks enveloped by pegmatitic hornblende in gabbro are reported from the Frog Lake pluton, Nova Scotia, Canada (Pe-piper, 2020). Lovering and Durrell (1959) also noted the resemblance of a similar inner zone of the pegmatites from Eureka Peak, Plumas County, California, to its wall rock, but finally rejected a xenolithic origin because the euhedral crystal faces indicate crystallization towards the core of the pockets. As the xenolith serves as a nucleation site, crystallization is expected to point outwards, away from the core. Similarly, in the zoned pegmatites of the mafic-ultramafic Hamn intrusion, the alignment of the small diopside grains on the fringe zone and the varying length of the larger grains towards the core indicate that the crystallization started from the outside and continued toward the core of the pockets (Fig. 6c, d), excluding the possibility of a xenolithic origin. Moreover, tonalites are expected to have higher concentrations of incompatible

elements, particularly REE, than the host rock. In contrast, the core of the zoned pegmatite has the lowest REE concentration of all zones. The negative Eu anomaly seen in the pegmatitic diopside layer but not in the host rock gabbronorites (Fig. 11c) suggests that the zoned pegmatite crystallized from an evolved residual melt that had already fractionated abundant plagioclase. The low REE concentrations of the core zone and the high REE concentrations of the pegmatitic pyroxene (Fig. 11d) suggest that massive crystallization of clinopyroxene in the pegmatitic zone consumed REEs, leaving the core of the pocket relatively depleted.

CONCLUSION

1. The unzoned pegmatites in the Palaeoproterozoic mafic–ultramafic Hamn intrusion and the associated rocks share an almost identical bulk composition, mineral assemblage characteristics, and mineral chemistry of the major mineral phases, indicating that the pegmatites did not crystallize from the intercumulus melt.
2. Plagioclase in the unzoned pegmatites and the host gabbro experienced epidotization and scapolitization. This most likely reflects the presence of a Cl-rich aqueous fluid phase during the late magmatic stage.
3. Some of the unzoned pegmatite pockets show tail-like attachments that merge into Cl-bearing pargasite dikelets surrounded by Cl-bearing scapolite, suggesting that crystallization of anhydrous minerals oversaturated the residual melt in H_2O and Cl and resulted in the phase separation. Consequently, the fluid pressure in the pegmatitic pockets could have exceeded the lithostatic pressure leading to the fracturing of the host rocks and the expulsion of the residual melt.

4. The high H_2O and Cl contents might have contributed to a reduced viscosity of the mafic melt, simultaneously increasing the diffusion rate and decreasing the nucleation rate (N) over the growth rate (G) and consequently favoring the growth of a few large crystals over the growth of numerous smaller crystals, i.e., promoting the development of pegmatitic texture.
5. The zoned pegmatites are internally differentiated in terms of grain size, texture, and mineralogy. Plagioclase of the core zone, between the pegmatitic diopside and in the fringe zone, is distinctly richer in sodium than plagioclase from the host gabbronorite.
6. The comb-like layering and bifurcating diopside grains indicate that the pegmatite-forming melt experienced undercooling. Due to the lack of evidence for H_2O diffusion and at plutonic setting, heat diffusion caused by the emplacement of remobilized intercumulus or fractionated melt (possibly from the nearby mafic/ultramafic cumulates) into the colder host gabbronorite is likely the mechanism that caused undercooling of the pegmatite-forming melt. A decrease of the initial degree of undercooling from the rim towards the core of the zoned pegmatite can explain the change from abundant small grains to fewer and larger diopside grains. Higher degrees of undercooling led to high nucleation rate vs growth rate ratios, resulting in numerous small grains, whereas lower degrees of undercooling caused lower nucleation rate vs growth rate ratios, resulting in the growth of fewer, larger grains.
7. Enrichment in CO_2 could have contributed to a reduced viscosity of the mafic melt and contributed to the development of pegmatitic textures.
8. The titanium-in-quartz geothermometer and the microthermometry of the CO_2-inclusions indicate a minimum formation temperature of 753 ± 34°C and

minimum formation pressure of 647 to 734 MPa for the quartz segregation zone of the zoned pegmatites.

AUTHOR CONTRIBUTION

All authors have read and agreed to the published version of the manuscript.

CRediT AUTHORSHIP CONTRIBUTION STATEMENT

Paul Heckmann: Conceptualization, Methodology, Formal analysis, Investigation, Writing - original draft, Visualization. **Sabina Strmić Palinkaš:** Conceptualization, Methodology, Investigation, Resources, Funding acquisition, Writing - review & editing, Project administration, Supervision. **Harald Hansen:** Writing - review & editing. **Giada Iacono-Marziano:** Writing - review & editing, Supervision. **Kristijan Rajič:** Investigation, Formal analysis, Writing - review & editing. **Melanie Forien:** Review & editing, Supervision. **Steffen G. Bergh:** Writing - review & editing.

ACKNOWLEDGEMENTS

The authors thank Muriel M. L. Erambert, Ida Di Carlo, Patricia Benoist-Julliot, Philippe Penhoud, Sylvain Janiec, Trine Dahl, Karina Monsen, and Ingvild Hald for their help with analytics and Saskia Erdmann for discussion. In addition, we thank Austin M. Gion, Carmen Braun and Jack J. Percival for proofreading the manuscript. Callum J. Hetherington, Rainer Thomas and two anonymous reviewers are greatly acknowledged for constructive reviews and suggestions for improving the article.

FUNDING

This research was funded by the Ph.D. project of the main author (Project number 301169). The open-access publication was funded by UiT, The Arctic University of Norway. Furthermore, this work was partly supported by the Research Council of

Norway through funding to the Norway Research School for Dynamics and Evolution of Earth and Planets (DEEP), project number 249040/F60. Further funding was provided by the committee for research training from UiT The Arctic University of Norway, grant number NTF-FU 116-19 and by the project A31566 at UiT The Arctic University of Norway.

SUPPLEMENTARY DATA

Tables of supplementary data are provided in the electronic appendix 1 and 2.

CONFLICTS OF INTERESTS

The authors declare no conflict of interest.

REFERENCES

Armitage, P., 2004. Structural geological reconnaissance in the Svanfjellet Shear Zone, Senja.le, Field report, Universitetet i Tromsø, Institutt for geologi.

Armitage, P., Bergh, S.G., 2005. Structural development of the Mjelde-Skorelwatn Zone on Kvaloya, Troms: A metasupracrustal shear belt in the Precambrian West Troms Basement Complex, North Norway. Nor. Geol. Tidsskr. 85, 117–132.

Bartels, A., Behrens, H., Holtz, F., Schmidt, B.C., Fechtelkord, M., Knipping, J., Crede, L., Baasner, A., Pukallus, N., 2013. The effect of fluorine, boron and phosphorus on the viscosity of pegmatite forming melts. Chem. Geol. 346, 184–198. https://doi.org/10.1016/j.chemgeo.2012.09.024

Bartels, A., Vetere, F., Holtz, F., Behrens, H., Linnen, R.L., 2011. Viscosity of flux-rich pegmatitic melts. Contrib. to Mineral. Petrol. 162, 51–60. https://doi.org/10.1007/s00410-010-0582-3

Beard, J.S., 1986. Characteristic mineralogy of arc-related cumulate gabbros: implications for the tectonic setting of gabbroic plutons and for andesite genesis. Geology 14, 848–851. https://doi.org/10.1130/0091-7613(1986)14<848:CMOACG>2.0.CO;2

Beard, J.S., Day, H., 1986. Origin of gabbro pegmatite in the Smartville intrusive complex, northern Sierra Nevada, California. Am. Mineral. 71, 1085–1099.

Beard, J.S., Fullagar, P.D., Sinha, A.K., 2002. Gabbroic pegmatite intrusions, Iberia Abyssal Plain, ODP Leg 173, Site 1070: Magmatism during a transition from non-volcanic rifting to sea-floor spreading. J. Petrol. 43, 885–905. https://doi.org/10.1093/petrology/43.5.885

Beard, J.S., Scott, S.R., 2018. A model for the high-temperature origin and paradoxical distribution of pegmatites in mafic plutons, Smartville Complex, California. J.

Petrol. 59, 3–10. https://doi.org/10.1093/petrology/egy015

Bergh, S.G., Corfu, F., Priyatkina, N., Kullerud, K., Myhre, P.I., 2015. Multiple post-Svecofennian 1750-1560Ma pegmatite dykes in Archaean-Palaeoproterozoic rocks of the West Troms Basement Complex, North Norway: Geological significance and regional implications. Precambrian Res. 266, 425–439. https://doi.org/10.1016/j.precamres.2015.05.035

Bergh, S.G., Eig, K., Kløvjan, O.S., Henningsen, T., Olesen, O., Hansen, J.A., 2007. The Lofoten-Vesterålen continental margin: A multiphase Mesozoic-Palaeogene rifted shelf as shown by offshore-onshore brittle fault-fracture analysis. Nor. Geol. Tidsskr. 87, 29–58.

Bergh, S.G., Haaland, L., Arbaret, L., Coint, N., Fabien, M., 2022. 1.80–1.75 Ga granite suites in the west Troms Basement Complex, northern Norway: Palaeoproterozoic magma emplacement during advancing accretionary orogeny, from field observations. Precambrian Res. 374, 106640. https://doi.org/10.1016/j.precamres.2022.106640

Bergh, S.G., Kullerud, K., Armitage, P.E.B., Zwaan, K.B., Corfu, F., Ravna, E.J.K., Myhre, P.I., 2010. Neoarchaean to svecofennian tectono-magmatic evolution of the West Troms Basement complex, North Norway. Nor. Geol. Tidsskr. 90, 21–48.

Boudreau, A.E., Mccallum, I.S., 1989. Contributions to Mineralogy and Petrology Investigations of the Stillwater Complex: Part V. Apatites as indicators of evolving fluid composition. Contrib Miner. Pet. 102, 138–153.

Brown, M., 2013. Granite: From genesis to emplacement. Bull. Geol. Soc. Am. 125, 1079–1113. https://doi.org/10.1130/B30877.1

Cawthorn, R.G., Boerst, K., 2006. Origin of the pegmatitic pyroxenite in the Merensky

Unit, Bushveld Complex, South Africa. J. Petrol. 47, 1509–1530. https://doi.org/10.1093/petrology/egl017

Corfu, F., 2013. A century of U-pb geochronology: The long quest towards concordance. Bull. Geol. Soc. Am. 125, 33–47. https://doi.org/10.1130/B30698.1

Corfu, F., 2007. Multistage metamorphic evolution and nature of the amphibolite-granulite facies transition in Lofoten-Vesterålen, Norway, revealed by U-Pb in accessory minerals. Chem. Geol. 241, 108–128. https://doi.org/10.1016/j.chemgeo.2007.01.028

Corfu, F., 2004. U-Pb age, setting and tectonic significance of the anorthosite-mangerite-charnockite-granite suite, Lofoten-Vesterålen, Norway. J. Petrol. 45, 1799–1819. https://doi.org/10.1093/petrology/egh034

Corfu, F., Armitage, P., Kullerud, K., Bergh, S.G., 2003. Preliminary U-Pb geochronology in the West Troms Basement Complex, North Norway: Archaean and Palaeoproterozoic events and younger overprints. Norges Geol. Undersokelse 441, 61–72

Devineau, K., Champallier, R., Pichavant, M., Etrology, P., Devineau, K., 2020. Dynamic crystallization of a haplogranitic melt: Application to pegmatites. J. Petrol. 61. https://doi.org/10.1093/petrology/egaa054

Diamond, L.W., 2001. Review of the systematics of CO2-H2O fluid inclusions. Lithos 55, 69–99. https://doi.org/10.1016/S0024-4937(00)00039-6

Fenn, P.M., 1977. The nucleation and growth of alkali feldspars from hydrous melts. Can. Mineral. 15, 135–161.

Glover, A.S., Rogers, W.Z., Barton, J.E., 2012. Granitic pegmatites: Storehouses of industrial minerals. Elements 8, 269–273. https://doi.org/10.2113/gselements.8.4.269

Goldsmith, J.R., 1982. Review of the behavior of plagioclase under metamorphic conditions. Am. J. Sci. 67, 643–652.

Goldsmith, J.R., Chicago, C., 1982. Plagioclase stability at elevated temperatures and water pressures. Am. Mineral. 67, 653–675.

Hanley, J.J., Gladney, E.R., 2011. The presence of carbonic-dominant volatiles during the crystallization of sulfide-bearing mafic pegmatites in the North Roby zone, Lac des Iles Complex, Ontario. Econ. Geol. 106, 33–54. https://doi.org/10.2113/econgeo.106.1.33

Hansen, H., Palinkaš, S.S., Bergh, S.G., Palinkaš, S.S., 2019. Proceeding of the 33rd Norwegian Geological Winter Meeting, Geological Society of Norway, in: Nakrem, H.A., Husås, A.M. (Eds.), Petrology, Ore Potential and Tectonic Setting of the Late-Svecofennian Hamn Intrusion, West Troms Basement Complex, North Norway. Geological Society of Norway, p. 31.

Hansteen, T.H., Klügel, A., 2008. Fluid inclusion thermobarometry as a tracer for magmatic processes. Rev. Mineral. Geochemistry 69, 143–177. https://doi.org/10.2138/rmg.2008.69.5

Henderson, I., Kendrick, M., 2003. Structural controls on graphite mineralisation, Senja, Troms. Geol. Surv. Norw. Rep. 111pp.

Högdahl, K., Andersson, U.B., Eklund, O., 2004. The transscandinavian Igneous Belt (TIB) in Sweden: A review of its character and evolution, Special Paper of the Geological Survey of Finland.

Jahns, R.H., Burnham, C.W., 1969. Experimental studies of pegmatite genesis: I. A model for the derivation and crystallization of granitic pegmatites. Econ. Geol. 64, 843–864. https://doi.org/10.2113/gsecongeo.64.8.843

Kullerud, K., Skjerlie, K.P., Corfu, F., de la Rosa, J.D., 2006. The 2.40 Ga Ringvassøy

mafic dykes, West Troms Basement Complex, Norway: The concluding act of early Palaeoproterozoic continental breakup. Precambrian Res. 150, 183–200. https://doi.org/10.1016/j.precamres.2006.08.003

Larsen, R.B., Brooks, C.K., 1994. Origin and evolution of gabbroic pegmatites in the skaergaard intrusion, East Greenland. J. Petrol. 35, 1651–1679. https://doi.org/10.1093/petrology/35.6.1651

Laurent, O., Vander Auwera, J., Bingen, B., Bolle, O., Gerdes, A., 2019. Building up the first continents: Mesoarchean to Paleoproterozoic crustal evolution in West Troms, Norway, inferred from granitoid petrology, geochemistry and zircon U-Pb/Lu-Hf isotopes. Precambrian Res. 321, 303–327. https://doi.org/10.1016/j.precamres.2018.12.020

Linnen, R.L., Van Lichtervelde, M., Černý, P., 2012. Granitic pegmatites as sources of strategic metals. Elements 8, 275–280. https://doi.org/10.2113/gselements.8.4.275

Lofgren, G., 1974. An experimental study of plagioclase crystal morphology; isothermal crystallization. Am. J. Sci. https://doi.org/10.2475/ajs.274.3.243

London, D., 2014. Subsolidus isothermal fractional crystallization. Am. Mineral. 99, 543–546. https://doi.org/10.1515/am.2014.4693

London, D., 2008. Pegmatites. Can. Miner. 10, 347.

London, D., 1984. Experimental phase equilibria in the system LiAlSiO4- SiO2-H2O: a petrogenetic grid for lithium-rich pegmatites. Am. Mineral. 69, 995–1004.

Lovering, J.K., Durrell, C., 1959. Zoned Gabbro Pegmatites of Eureka Peak, Plumas County, California. J. Geol. 67, 253–268. https://doi.org/10.1086/626582

Mastin, L.G., Ghiorso, M.S., 2001. Adiabatic temperature changes of magma-gas mixtures during ascent and eruption. Contrib. to Mineral. Petrol. 141, 307–321.

https://doi.org/10.1007/s004100000210

Mathez, E.A., Waight, T.E., 2003. Lead isotopic disequilibrium between sulfide and plagioclase in the Bushveld Complex and the chemical evolution of large layered intrusions. Geochim. Cosmochim. Acta 67, 1875–1888. https://doi.org/10.1016/S0016-7037(02)01294-2

McDonough, W.F., Sun, S.-S. s., 1995. The composition of the Earth. Chem. Geol. 120, 223–253. https://doi.org/10.1016/0009-2541(94)00140-4

Meurer, W.P., Boudreau, A.E., 1996. An evaluation of models of apatite compositional variability using apatite from the Middle Banded Series of the Stillwater Complex, Montana. Contrib. to Mineral. Petrol. 125, 225–236. https://doi.org/10.1007/s004100050218

Mutchler, S.R., Fedele, L., Bodnar, R.J., 2008. Analysis Management System (AMS) for reduction of laser ablation ICPMS data. In Laser-Ablation-ICPMS in the Earth Sciences: Current Practices and Outstanding Issues (ed. P. Sylvester). Miner. Assoc Canada, Quebec. https://doi.org/10.2113/gsecongeo.104.4.601

Myhre, P.I., Corfu, F., Bergh, S.G., Kullerud, K., 2013. U-Pb geochronology along an Archaean geotransect in the West Troms Basement Complex, North Norway. Nor. Geol. Tidsskr. 93, 1–24.

Mysen, B.O., Richet, P., 2005. Silicate Melts—Properties and Structure, 544 p.

Nabelek, P.I., Whittington, A.G., Sirbescu, M.L.C., 2010. The role of H2O in rapid emplacement and crystallization of granite pegmatites: Resolving the paradox of large crystals in highly undercooled melts. Contrib. to Mineral. Petrol. 160, 313–325. https://doi.org/10.1007/s00410-009-0479-1

Pe-piper, G., 2020. Mineralogy of an Appinitic Hornblende Gabbro and Its Significance for the Evolution of Rising Calc-Alkaline Magmas. Minerals.

Péntek, A., Molnár, F., Watkinson, D.H., 2006. Magmatic fluid segregation and overprinting hydrothermal processes in gabbro pegmatites of the Neotethyan ophiolitic Szarvaskö Complex (Bükk Mountains, NE Hungary). Geol. Carpathica 57, 433–446.

Pistone, M., Blundy, J.D., Brooker, R.A., EIMF, 2016. Textural and chemical consequences of interaction between hydrous mafic and felsic magmas: an experimental study. Contrib. to Mineral. Petrol. 171, 1–21. https://doi.org/10.1007/s00410-015-1218-4

Pitzer, K.S., Sterner, S.M., 1994. Equations of state valid continuously from zero to extreme pressures for H2O and CO2. J. Chem. Phys. 101, 3111–3116. https://doi.org/10.1063/1.467624

Scoon, R.N., Mitchell, A.A., 2004. The platiniferous dunite pipes in the eastern limb of the Bushveld Complex: Review and comparison with unmineralized discordant ultramafic bodies. South African J. Geol. 107, 505–520. https://doi.org/10.2113/107.4.505

Shaw, H.R., 1963. Obsidian-H 2 O viscosities at 1000 and 2000 bars in the temperature range 700° to 900°C . J. Geophys. Res. 68, 6337–6343. https://doi.org/10.1029/jz068i023p06337

Simmons, W.B., 2007. Pegmatite genesis: Recent advances and area for future research. Granitic pegmatites state art - Int. Symp.

Simmons, W.B., Pezzotta, F., Shigley, J.E., Beurlen, H., 2012. Granitic pegmatites as sources of colored gemstones. Elements 8, 281–287. https://doi.org/10.2113/gselements.8.4.281

Simmons, W.B., Webber, K., 2008. Pegmatite genesis: state of the art. Eur. J. Mineral. 20, 421–438. https://doi.org/10.1127/0935-1221/2008/0020-1833

Sirbescu, M.L.C., Schmidt, C., Veksler, I. V., Whittington, A.G., Wilke, M., 2017. Experimental crystallization of undercooled felsic liquids: Generation of pegmatitic texture. J. Petrol. 58, 539–568. https://doi.org/10.1093/petrology/egx027

Sonnenthal, E.L., 1992. Geochemistry of dendritic anorthosites and associated pegmatites in the Skaergaard Intrusion, East Greenland: Evidence for metasomatism by a chlorine-rich fluid. J. Volcanol. Geotherm. Res. 52, 209–230. https://doi.org/10.1016/0377-0273(92)90141-Y

Span, R., Wagner, W., 1996. A new equation of state for carbon dioxide covering the fluid region from the triple-point temperature to 1100 K at pressures up to 800 MPa. J. Phys. Chem. Ref. Data 25, 1509–1596. https://doi.org/10.1063/1.555991

Strmić Palinkaš, S., Bermanec, V., Palinkaš, L.A., Boev, B., Gault, R.A., Prochaska, W., Bakker, R.J., 2012. The evolution of the čanište epidote-bearing pegmatite, Republic of Macedonia: evidence from mineralogical and geochemical features. Geol. Croat. 65, 423–434.

Sunde, Ø., Friis, H., Andersen, T., 2018. Variation in major and trace elements of primary wöhlerite as an indicator of the origin of Pegmatites in the Larvik plutonic complex, Norway. Can. Mineral. 56, 529–542. https://doi.org/10.3749/canmin.1700050

Suzuki, A., 2018. Effect of carbon dioxide on the viscosity of a melt of jadeite composition at high pressure. J. Mineral. Petrol. Sci. 113, 47–50. https://doi.org/10.2465/jmps.170717

Swanson, S.E., 1977. Relation of nucleation and crystal-growth rate to the development of granitic textures. Am. Mineral. 62, 966–978.

Thomas, R., Davidson, P., 2012. Water in granite and pegmatite-forming melts. Ore Geol. Rev. 46, 32–46. https://doi.org/10.1016/j.oregeorev.2012.02.006

Thomas, R., Heinrich, W., Förster, H.J., Heinrich, W., Foerster, H.-J., Heinrich, W., 2003. The behaviour of boron in a peraluminous granite-pegmatite system and associated hydrothermal solutions: A melt and fluid-inclusion study. Contrib. to Mineral. Petrol. 144, 457–472. https://doi.org/10.1007/s00410-002-0410-5

Van Den Kerkhof, A., Thiéry, R., 2001. Carbonic inclusions. Lithos 55, 49–68. https://doi.org/10.1016/S0024-4937(00)00038-4

Vasyukova, O., Williams-Jones, A.E., 2014. Fluoride-silicate melt immiscibility and its role in REE ore formation: Evidence from the Strange Lake rare metal deposit, Québec-Labrador, Canada. Geochim. Cosmochim. Acta 139, 110–130. https://doi.org/10.1016/j.gca.2014.04.031

Vernon, R., 2018. A Practical Guide to Rock Microstructure, Second Edi. ed. Cambrdinge Universtiy Press. https://doi.org/10.1017/9781108654609

Vernon, R., 1985. Possible role of superheated magma in the formation of orbicular granitoids. Geology 13, 843–845

Viljoen, M.J., Scoon, R.N., 1985. The distribution and main geologic features of discordant bodies of iron-rich ultramafic pegmatite in the Bushveld complex. Econ. Geol. 80, 1109–1128. https://doi.org/10.2113/gsecongeo.80.4.1109

Wark, D.A., Watson, E.B., 2006. TitaniQ: A titanium-in-quartz geothermometer. Contrib. to Mineral. Petrol. 152, 743–754. https://doi.org/10.1007/s00410-006-0132-1

Watson, E.B., Baker, D.R., 1991. Chemical Diffusion in Magmas: An Overview of Experimental Results and Geochemical Applications 120–151. https://doi.org/10.1007/978-1-4612-3128-8_4

Webb, S.L., Murton, B.J., Wheeler, A.J., 2014. Rheology and the Fe3+-chlorine reaction in basaltic melts. Chem. Geol. 366, 24–31.

https://doi.org/10.1016/j.chemgeo.2013.12.006

Whitney, D.L., Evans, B.W., 2010. Abbreviations for names of rock-forming minerals. Am. Mineral. 95, 185–187. https://doi.org/10.2138/am.2010.3371

Zellmer, G.F., Edmonds, M., Straub, S.M., 2015. Volatiles in subduction zone magmatism. Geol. Soc. Spec. Publ. 410, 1–17. https://doi.org/10.1144/SP410.13

Zhang, J., Lee, C.T.A., 2020. Disequilibrium crystallization and rapid crystal growth: a case study of orbicular granitoids of magmatic origin. Int. Geol. Rev. 00, 1–17. https://doi.org/10.1080/00206814.2020.1734975

Zwaan, K.B., 1995. Geology of the West Troms Basement Complex, northern Norway, with emphasis on the Senja Shear Belt: a preliminary account. Geol. Surv. Norw. Bull. 427, 33–36.

Zwaan, K.B., Fareth, E., 2005. Berggrunnskart MEFJORDBOTN 1433 IV, M 1:50 000, foreøpig utgave. Norges Geol. undersøkelse.

FIGURE CAPTIONS

Fig. 1. (a) Geological map of Fennoscandia, after Bergh et al. (2010) . The West Troms Basement Complex (WTBC) is highlighted by the red rectangle in the north of Norway; (b) Regional geologic-tectonic map of the WTBC (modified after Bergh et al., 2015, 2010; Laurent et al., 2019; Myhre et al., 2013; Zwaan, 1995). The Hamn intrusion is located on the western shore in the center of Senja (see red rectangle).

Fig. 2. (a) Map of the mafic-ultramafic Hamn intrusion. The red rectangle highlights the sample location in the north of the intrusion; (b) Overview map of the sample locations. The red star illustrates the sample area of the unzoned pegmatites around

the Hotel I Senja, whereas the green star shows the location of the zoned pegmatites at the tip of the peninsular Hellandsneset; (c) shows are more detailed map of Hellandsneset, illustrating the position of the zoned pegmatites between the Biotite norite and the Biotite metagabbro.

Fig. 3. Illustration of the position of thin section sampling of the sample PH-HM-32, which presents the transition of fine grained host gabbro and pegmatite. T1 and T2 represent thin section taken from the gabbro, whereas T4 and T5 represent the pegmatitic part of the sample. T3 is a thin section taken between the gabbro and pegmatite.

Fig. 4. Photographs of unzoned pegmatite pockets in the outcrop and of sample PH-HM-32: (a) Pegmatitic pocket differs from the host gabbronorite only by a smooth coarsening of the grain size (lens protection is ca. 45 mm); (b) Close-up of the same pegmatitic body seen in (a) shows the central dyke-like feature striking sharply through the pocket from the lower left to the upper right side; (c) Pegmatite pocket associated with an pargasite dyke. (d) Sample PH-HM-32, representing the transition from a fine-grained gabbro to a gabbroic pegmatite.

Fig. 5. Photographs of zoned pegmatites in outcrop and corresponding schematic sketches illustrating the different zones of the pockets; (a) Isometric pegmatite pocket with a small core zone; (b) Elongated pegmatite pocket. (c) Largest pocket of the zoned pegmatite. Note that the additional quartz segregation zone and mafic dikelets in the core are absent in the other zoned pegmatite pockets in (a) and (c).

Fig. 6. Outcrop photographs of features from the zoned pegmatite; (a) Large, zoned pegmatite pocket (Folding rule is 2 m long). The inlet highlights the outline of the pocket. Note the meandering outline on the right side of the pocket; (b) Mafic dikelets inside the core zone of the large, zoned pegmatite pocket. The inlet represents the shape of the dikelets; (c) Comb-like layer diopside. Note the change from small but numerous, aligned diopside grains to large but fewer diopside grains (Pen is ca. 12 cm long); (d) Comb-like layer diopside grains from medium-sized pocket (Fig. 5b).

Fig. 7. Microphotographs of thin-sections from unzoned pegmatite and their host rocks (in plane-parallel light, PPL); (a) Plagioclase without epidotization associated with pargasite and biotite in the host gabbronorite (KR-HM-28); (b) Biotite near the pargasitic amphibole rim in host gabbronorite (KR-HM-28); (c) Pargasite dikelet surrounded by fine-grained scapolite in host gabbronorite (KR-HM-24); (d) Epidotization and scapolitization in the host gabbro (T1 in PH-HM-32); (e) Fibrous sillimanite in scapolite in the host gabbro (T1 in PH-HM-32); (f) Mineral assemblage in unzoned pegmatite; (g) Epidotization of plagioclase and scapolitization at the contact between plagioclase and clinopyroxene (T4 in PH-HM-32); (h) Ilmenite surrounded by interstitial garnet between plagioclase. Also, note the heterogeneous distribution of zoisite in the plagioclase (T5 in PH-HM-32); (i) Symplectitic intergrowth of orthopyroxene and Fe-oxide (KR-HM-35); (j) Sulfide assemblage of pyrrhotite and pyrite in clinopyroxene (KR-HM-36); (k) Ilmenite is surrounded by garnet and biotite within the pargasitic amphibole rim (KR-HM-36); (l) Apatite within pargasitic amphibole rim (T5 in PH-HM-32). Mineral abbreviations after Whitney and Evans (2010).

Fig. 8. (a) Plagioclase composition of unzoned pegmatites (beams indicate the range, vertical order is arbitrary); (b) Pyroxene composition of unzoned pegmatites.

Fig. 9. Microphotographs of thin sections from different parts of the zoned pegmatite and its associated host rocks: (a) Stratigraphically lower host Biotite-norite (PH-HM-26); (b) Stratigraphically upper host Metagabbro (PH-HM-25); (c) Fringe zone (PH-HM-29); (d) Diopside from the pegmatitic diopside zone (PH-HM-28); (e) Quartz segregation zone with adjacent feldspar (PH-HM-24); (f) Core zone (PH-HM-22). Mineral abbreviations after Whitney and Evans (2010).

Fig. 10. (a) Plagioclase composition from different zones of the zoned pegmatite; (b) Pyroxene composition from pegmatitic and fringe zone of the zoned pegmatite.

Fig. 11. Pyrolite (McDonough and Sun (1995) normalized REE pattern. (a) Whole rock REE pattern of host gabbronorite and gabbronorite pegmatite; (b) REE pattern of plagioclase and pyroxene from host gabbronorite and gabbronorite pegmatite; (c) REE pattern from whole-rock samples each zone from the large, zoned pegmatite pocket (Fig. 5c) and host rock; (d) REE pattern of plagioclase and pyroxene from the pegmatitic zone of the zoned pegmatite.

Fig. 12: (a) Photomicrograph of a cluster of CO_2 fluid inclusions hosted by quartz; (b) Photomicrograph of a growth zone in quartz marked by CO_2 fluid inclusions; (c) Photomicrograph of a cluster of CO_2 fluid inclusions hosted by pyroxene; (d) Raman spectra of a representative CO_2 fluid inclusion hosted by quartz.

Fig. 13: The proposed link between the change in texture with a decreasing degree of undercooling and the typical curves for variation of nucleation rate (N) and growth rate (G). The diagram on the left side is simplified after Vernon (2018).

Table 1: Major elements of pegmatites and associated host rocks in wt. %.

	Unzoned pegmatite		Zoned pegmatite					
Sample	Gabbronorite	Pegmatite	Bt metagabbro[c]	Bt norite[d]	Fringe	Diopside	Diopside zone	Core
Label	KR-HM-28	KR-HM-36	PH-HM-25	PH-HM-26	PH-HM-29	PH-HM-28	PH-HM-27	PH-HM-22
SiO_2	52.19	51.55	52.27	53.55	55.88	59.76	61.11	71.75
TiO_2	0.48	0.32	0.63	0.69	0.65	0.36	0.28	0.14
Al_2O_3	20.05	20.3	16.76	16.9	14.55	5.10	9.12	14.94
Fe_2O_3[a]	6.72	5.84	7.81	8.44	9.37	12.64	7.77	1.77
MnO	0.08	0.08	0.11	0.12	0.10	0.15	0.12	0.02
MgO	5.5	6.34	6.24	6.13	5.39	10.68	7.72	0.56
CaO	10.69	10.66	8.78	8.56	7.55	8.62	9.40	1.26
Na_2O	3.45	3.53	4.45	3.63	5.15	2.20	4.00	7.34
K_2O	0.35	0.36	1.41	1.41	0.62	0.22	0.32	0.41
P_2O_5	0.03	0.04	0.52	0.41	0.46	0.04	0.06	0.10
LOI[b]	0.59	0.79	0.53	0.63	0.51	0.94	0.73	0.50
Total	100.10	99.80	99.51	100.50	100.20	100.70	100.60	98.78

Analyses carried out via whole rock FUS-ICP.
Fe_2O_3[a] indicate total Fe as Fe_2O_3.
LOI[b] indicates Loss Of Ignition.
Bt metagabbro[c] indicates the stratigraphically upper host rock.
Bt norite[d] indicates the stratigraphically lower host rock.

Table 2: Trace elements of pegmatites and associated host rocks in ppm.

Type		Unzoned pegmatite		Zoned pegmatite					
Sample		Gabbronorite	Pegmatite	Bt metagabbro[a]	Bt norite[b]	Fringe	Diopside	Diopside zone	Core
Label	Method	KR-HM-28	KR-HM-36	PH-HM-25	PH-HM-26	PH-HM-29	PH-HM-28	PH-HM-27	PH-HM-22
Cr	FUS-MS	80	180	120	80	400	130	70	40
Co	FUS-MS	29	32	33	39	31	38	28	3
Ni	FUS-MS	30	70	120	100	170	130	140	<20
Cu	FUS-MS	20	50	20	80	<10	20	40	20
Zn	FUS-MS	40	30	70	90	70	90	70	<30
Ga	FUS-MS	17	15	17	18	19	12	15	21
Ge	FUS-MS	1.3	1.3	1.3	1.2	1.5	2.7	2.2	0.9
Rb	FUS-MS	2	2	31	44	15	2	3	6
Y	FUS-MS	6.2	6.4	19.7	14.2	24.7	22.3	22.4	6.4
Nb	FUS-MS	0.5	0.8	9.9	7.1	8.5	5	4	2.1
Sn	FUS-MS	<1	<1	167	54	96	39	247	88
La	FUS-MS	4.5	4.75	37.1	30.5	45.3	12.4	22.1	8.73
Ce	FUS-MS	9.65	10.1	80.3	61.8	93.2	41.5	52.4	22.3
Pr	FUS-MS	1.23	1.25	9.78	7.06	10.8	6.55	6.96	2.98
Nd	FUS-MS	5.51	5.32	38.7	27.3	41.6	28.6	29.9	12.2
Sm	FUS-MS	1.17	1.17	6.91	4.71	7.46	6.41	6.29	2.25
Eu	FUS-MS	0.742	0.634	2.12	1.49	2.12	1.61	1.31	0.684
Gd	FUS-MS	1.07	1.17	5.38	3.68	5.97	5.25	5.4	1.63
Tb	FUS-MS	0.18	0.19	0.74	0.52	0.9	0.76	0.8	0.26

Dy	FUS-MS	1.1	1.16	3.85	2.69	4.56	4.2	4.27	1.3
Ho	FUS-MS	0.23	0.22	0.7	0.52	0.86	0.81	0.82	0.24
Er	FUS-MS	0.65	0.61	1.88	1.37	2.45	2.37	2.21	0.72
Tm	FUS-MS	0.094	0.088	0.27	0.193	0.351	0.335	0.328	0.097
Yb	FUS-MS	0.59	0.55	1.7	1.25	2.21	2.3	2.25	0.66
Lu	FUS-MS	0.084	0.077	0.265	0.197	0.348	0.372	0.362	0.106
Hf	FUS-MS	0.4	0.5	3.6	2.9	5.7	7.4	6.7	3.8
Ta	FUS-MS	<0.01	0.04	0.79	0.47	0.71	1.39	1.04	0.73
W	FUS-MS	<0.5	<0.5	15.2	5.6	8.9	4	22.9	9.1
Th	FUS-MS	0.22	0.4	3.26	4.02	4.58	7.84	14.5	33.7
U	FUS-MS	0.09	0.17	0.83	0.9	1.54	2.06	2.82	5.23
Sc	FUS-ICP	21	22	18	20	27	48	28	3
V	FUS-ICP	52.19	51.55	66	98	125	129	80	15
Sr	FUS-MS	20.05	20.3	727	747	443	76	193	203
Zr	FUS-ICP	6.72	5.84	136	102	209	209	179	106
Ba	FUS-ICP	0.08	0.077	702	780	250	36	75	76

FUS-ICP = Fusion Inductively coupled plasma, FUS-MS = Fusion Mass Spectrometry
< symbol indicates values below detection limit.
Bt metagabbro[a] indicates the stratigraphically upper host rock.
Bt norite[b] indicates the stratigraphically lower host rock.

Table 3: Trace element composition of grain separates in ppm.

Type		Unzoned pegmatite				Zoned pegmatite	
Lithology		Gabbronorite		Pegmatite		Pegmatite	
Mineral		Plagioclase	Pyroxene	Plagioclase	Pyroxene	Plagioclase	Pyroxene
Label	Method	KR-HM-28 pg	KR-HM-28 px	KR-HM-36 pg	KR-HM-36 px	PH-HM-27 Pg	PH-HM-27 Px
V	FUS-ICP	8	332	< 5	248	< 5	102
Cr	FUS-MS	< 20	190	< 20	280	< 20	100
Co	FUS-MS	3	55	2	40	1	39
Ni	FUS-MS	< 20	60	< 20	[illegible]	< 20	210
Cu	FUS-MS	< 10	10	50	40	< 10	10
Zn	FUS-MS	< 30	80	< 30	60	< 30	90
Ga	FUS-MS	18	12	[illegible]	11	23	9
Ge	FUS-MS	0.8	2.2	1.2	1.8	0.8	3.4
Rb	FUS-MS	< 1	3	< 1	< 1	1	2
Sr	FUS-MS	1270	[illegible]	1290	92	315	33
Y	FUS-MS	0.8	15.9	1.1	21.6	1.2	29.9
Zr	FUS-ICP	3	29	8	36	40	88
Nb	FUS-MS	< 0.2	1	< 0.2	4	0.2	2.1
Ba	FUS-ICP	302	142	346	95	115	27
La	FUS-MS	5.08	3.71	5.22	3.42	2.88	15.5
Ce	FUS-MS	8.55	11.1	9	11.2	5.45	45.7
Pr	FUS-MS	0.85	1.86	0.95	2	0.72	7.08
Nd	FUS-MS	2.92	9.41	3.21	10.8	2.95	32.4
Sm	FUS-MS	0.35	2.62	0.42	3.4	0.53	8.27

Eu	FUS-MS	0.678	0.846	0.69	0.933	0.215	1.35
Gd	FUS-MS	0.27	2.93	0.26	3.9	0.29	7.41
Tb	FUS-MS	0.03	0.5	0.04	0.65	0.05	1.1
Dy	FUS-MS	0.14	2.89	0.23	3.93	0.27	5.88
Ho	FUS-MS	0.03	0.56	0.04	0.75	0.05	1.09
Er	FUS-MS	0.06	1.54	0.1	2.14	0.14	3.03
Tm	FUS-MS	0.008	0.22	0.013	0.291	0.02	0.443
Yb	FUS-MS	0.05	1.44	0.08	1.83	0.14	2.99
Lu	FUS-MS	0.008	0.227	0.012	0.265	0.023	0.48
Hf	FUS-MS	< 0.1	1	0.2	1.2	1.1	4.1
Ta	FUS-MS	< 0.01	0.04	< 0.01	0.34	0.1	0.4
Th	FUS-MS	0.19	0.36	0.32	0.52	1.03	1.83
U	FUS-MS	0.06	0.15	0.12	0.4	0.29	0.86

FUS-ICP = Fusion Inductively coupled plasma, FUS-MS = Fusion Mass Spectrometry
< symbol indicates values below detection limit.

Declaration of interests

☒ The authors declare that they have no known competing financial interests or personal relationships that could have appeared to influence the work reported in this paper.

☐The authors declare the following financial interests/personal relationships which may be considered as potential competing interests:

HIGHLIGHTS

- The mafic-ultramafic Hamn intrusion hosts unzoned and zoned gabbroic pegmatites
- The unzoned pegmatites crystallized from a H_2O and Cl rich mafic melt
- Change in degree of undercooling led to a comb-like texture of the zoned pegmatites
- The zoned pegmatites crystallized from a dry but CO_2-enriched mafic melt

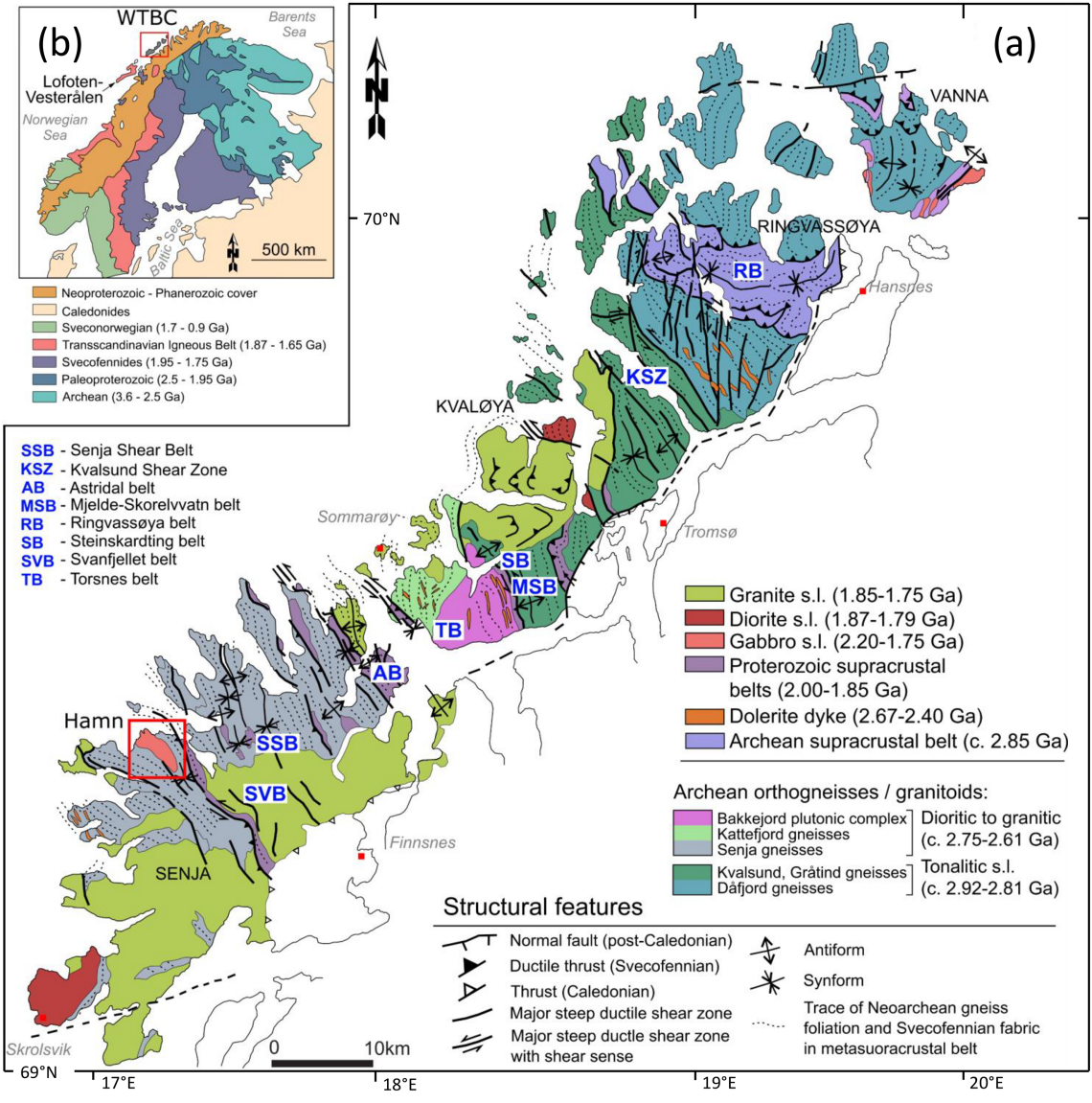
(b)
WTBC
Barents Sea
Lofoten-Vesterålen
Norwegian Sea
Baltic Sea
500 km
Neoproterozoic - Phanerozoic cover
Caledonides
Sveconorwegian (1.7 - 0.9 Ga)
Transscandinavian Igneous Belt (1.87 - 1.65 Ga)
Svecofennides (1.95 - 1.75 Ga)
Paleoproterozoic (2.5 - 1.95 Ga)
Archean (3.6 - 2.5 Ga)
(a)
VANNA
70°N
RINGVASSØYA
RB
Hansnes
KSZ
KVALØYA
Sommarøy
Tromsø
SB
MSB
TB
AB
Hamn
SSB
SVB
SENJA
Finnsnes
Skrolsvik
69°N
17°E
18°E
19°E
20°E
0
10km
SSB - Senja Shear Belt
KSZ - Kvalsund Shear Zone
AB - Astridal belt
MSB - Mjelde-Skorelvvatn belt
RB - Ringvassøya belt
SB - Steinskardting belt
SVB - Svanfjellet belt
TB - Torsnes belt
Granite s.l. (1.85-1.75 Ga)
Diorite s.l. (1.87-1.79 Ga)
Gabbro s.l. (2.20-1.75 Ga)
Proterozoic supracrustal belts (2.00-1.85 Ga)
Dolerite dyke (2.67-2.40 Ga)
Archean supracrustal belt (c. 2.85 Ga)
Archean orthogneisses / granitoids:
Bakkejord plutonic complex
Kattefjord gneisses
Senja gneisses
Dioritic to granitic (c. 2.75-2.61 Ga)
Kvalsund, Gråtind gneisses
Dåfjord gneisses
Tonalitic s.l. (c. 2.92-2.81 Ga)
Structural features
Normal fault (post-Caledonian)
Ductile thrust (Svecofennian)
Thrust (Caledonian)
Major steep ductile shear zone
Major steep ductle shear zone with shear sense
Antiform
Synform
Trace of Neoarchean gneiss foliation and Svecofennian fabric in metasuoracrustal belt

Figure 1

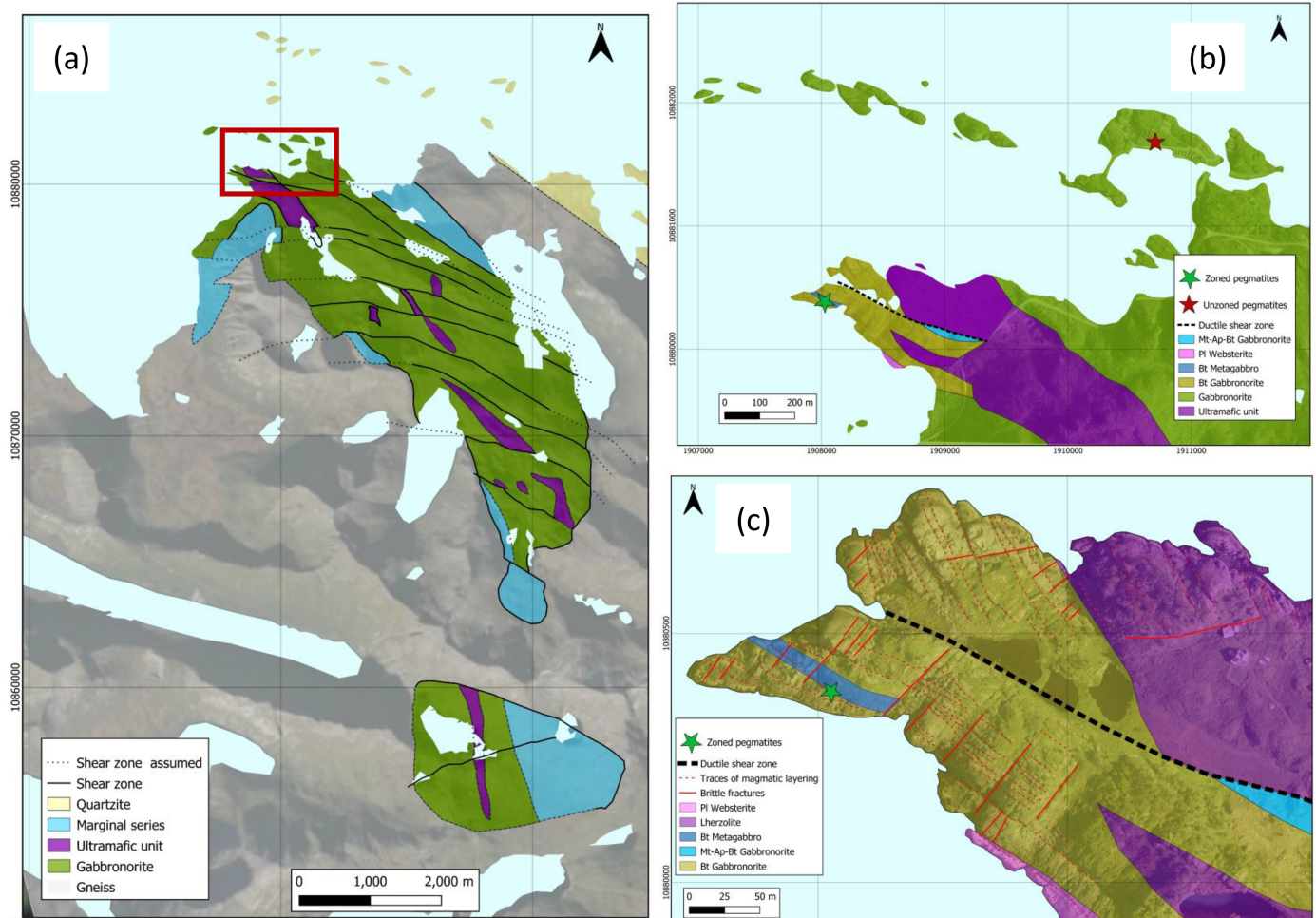
(a)
N
Shear zone assumed
Shear zone
Quartzite
Marginal series
Ultramafic unit
Gabbronorite
Gneiss
0 1,000 2,000 m
10880000
10870000
10860000
1900000
1910000
1920000
(b)
N
Zoned pegmatites
Unzoned pegmatites
Ductile shear zone
Mt-Ap-Bt Gabbronorite
Pl Websterite
Bt Metagabbro
Bt Gabbronorite
Gabbronorite
Ultramafic unit
0 100 200 m
10882000
10881000
10880000
1907000
1908000
1909000
1910000
1911000
(c)
N
Zoned pegmatites
Ductile shear zone
Traces of magmatic layering
Brittle fractures
Pl Websterite
Lherzolite
Bt Metagabbro
Mt-Ap-Bt Gabbronorite
Bt Gabbronorite
0 25 50 m
10880500
10880000
1908000
1908500

Figure 2

Figure 3

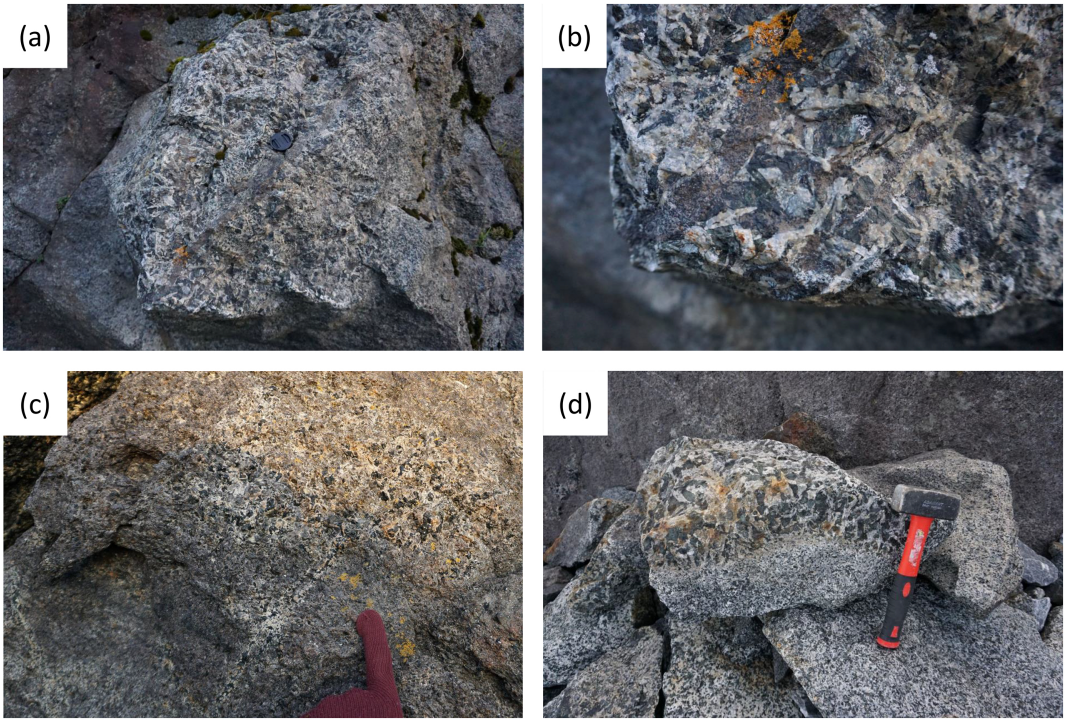

Figure 4

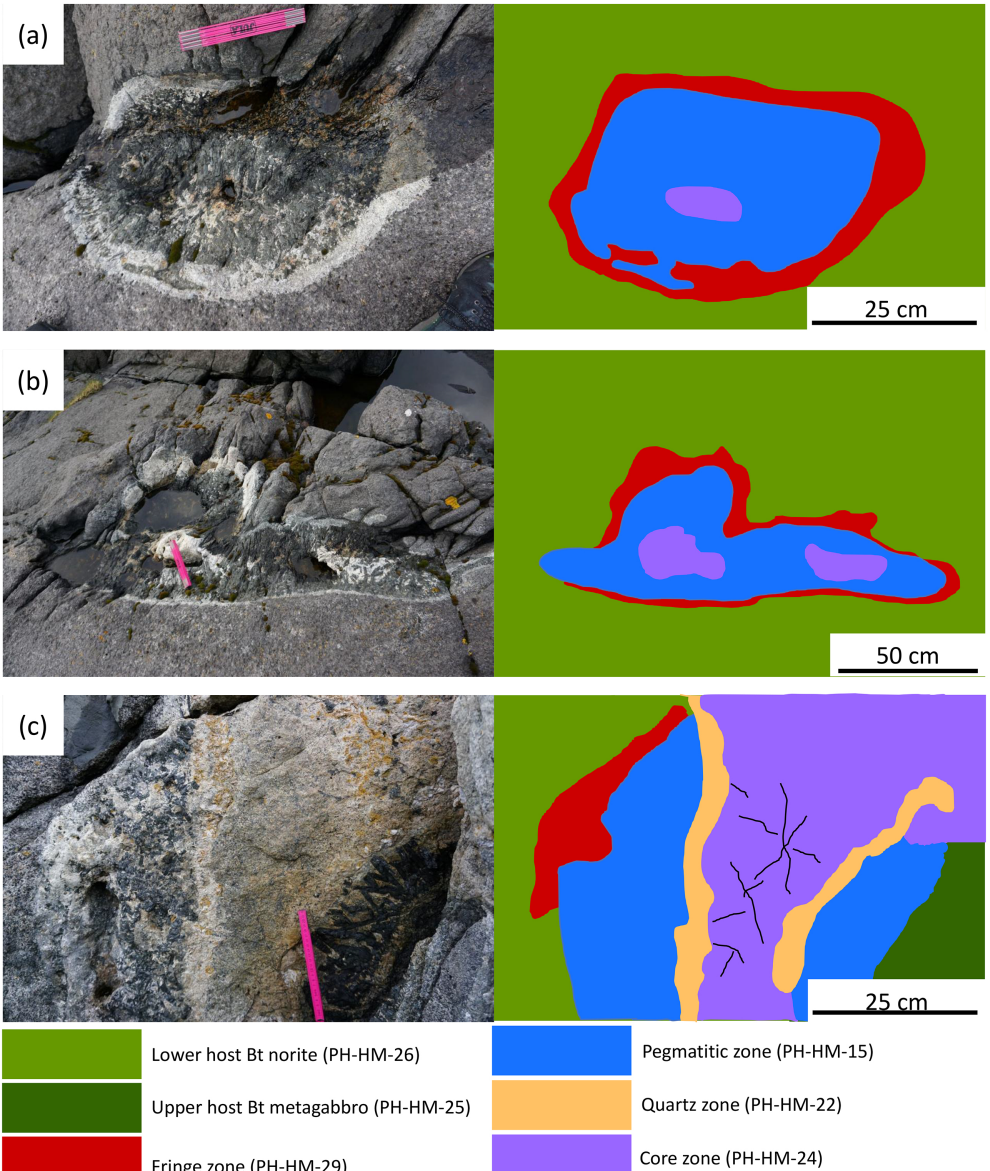
(a)
25 cm
(b)
50 cm
(c)
25 cm
Lower host Bt norite (PH-HM-26)
Upper host Bt metagabbro (PH-HM-25)
Fringe zone (PH-HM-29)
Pegmatitic zone (PH-HM-15)
Quartz zone (PH-HM-22)
Core zone (PH-HM-24)

Figure 5

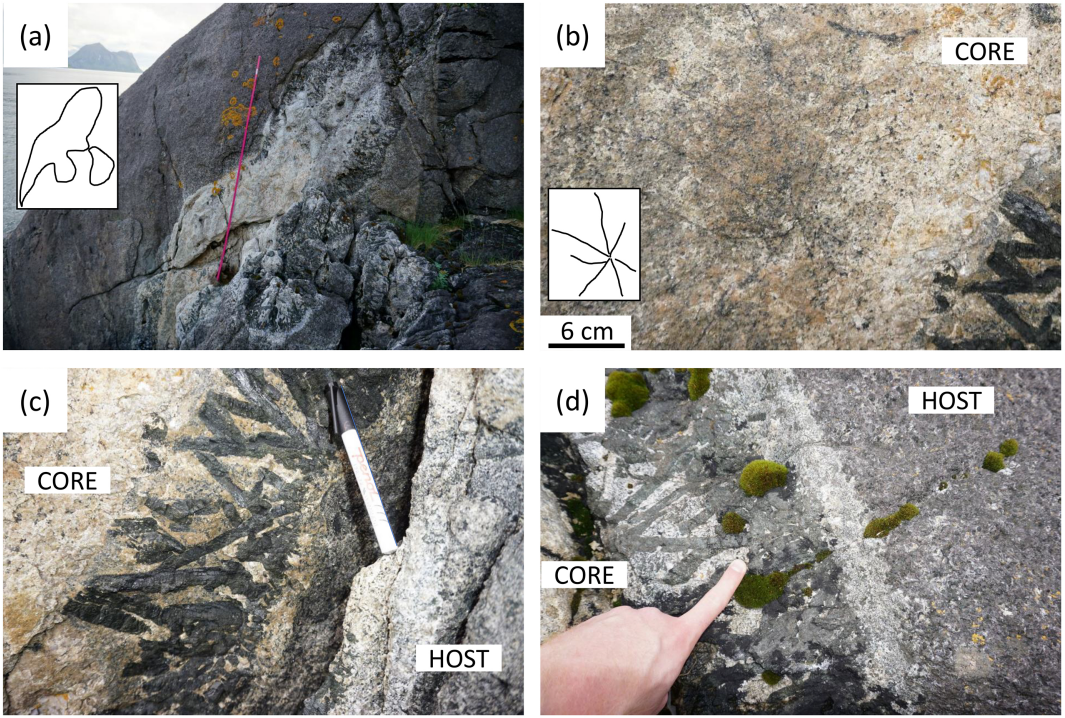

Figure 6

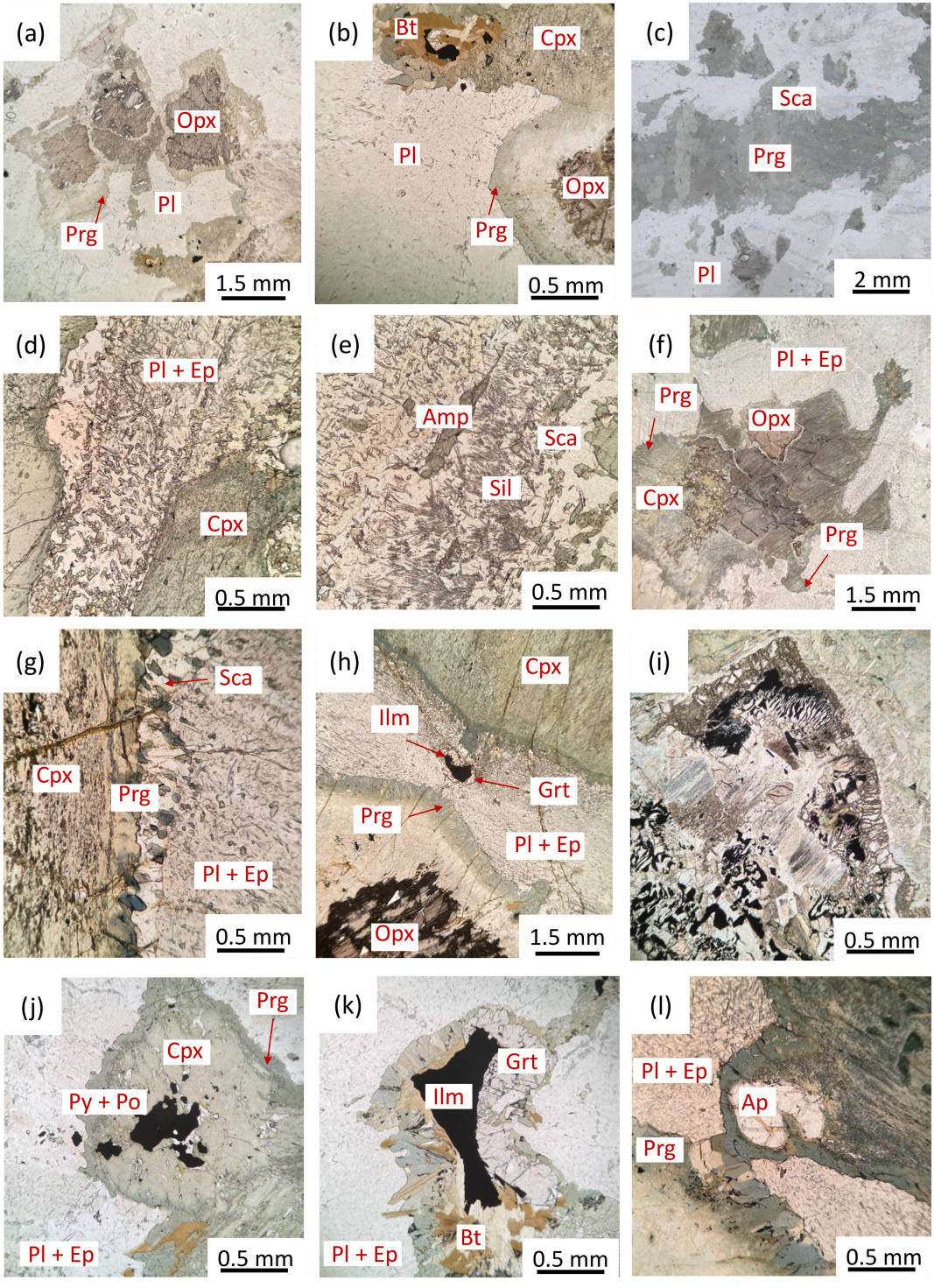
(a)
Opx
Pl
Prg
1.5 mm
(b)
Bt
Cpx
Pl
Opx
Prg
0.5 mm
(c)
Sca
Prg
Pl
2 mm
(d)
Pl + Ep
Cpx
0.5 mm
(e)
Amp
Sca
Sil
0.5 mm
(f)
Pl + Ep
Prg
Opx
Cpx
Prg
1.5 mm
(g)
Sca
Cpx
Prg
Pl + Ep
0.5 mm
(h)
Cpx
Ilm
Grt
Prg
Pl + Ep
Opx
1.5 mm
(i)
0.5 mm
(j)
Prg
Cpx
Py + Po
Pl + Ep
0.5 mm
(k)
Grt
Ilm
Pl + Ep
Bt
0.5 mm
(l)
Pl + Ep
Ap
Prg
0.5 mm

Figure 7

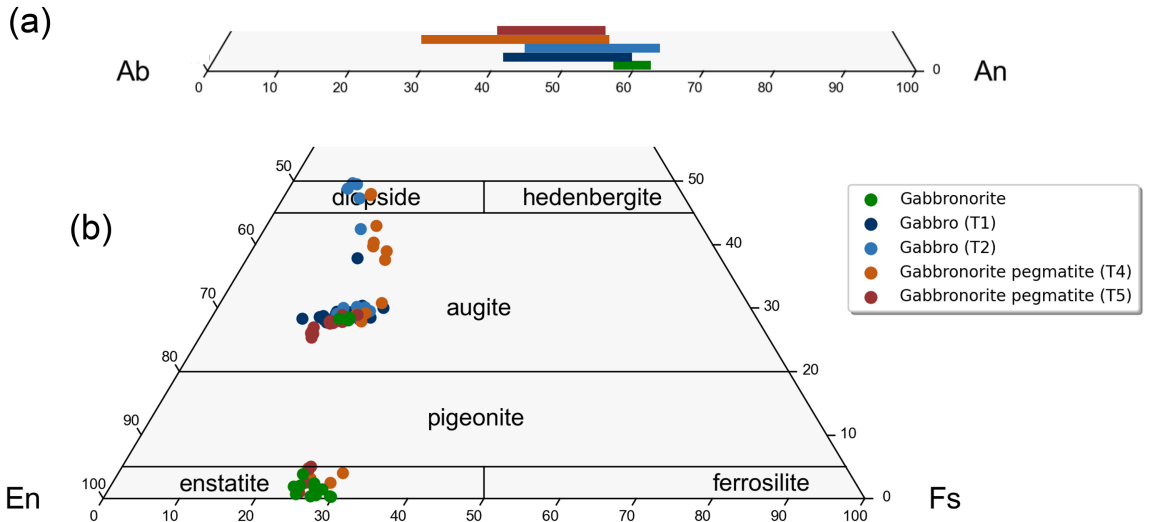
(a)
Ab
An
0
10
20
30
40
50
60
70
80
90
100
(b)
diopside
hedenbergite
augite
pigeonite
enstatite
ferrosilite
En
Fs
Gabbronorite
Gabbro (T1)
Gabbro (T2)
Gabbronorite pegmatite (T4)
Gabbronorite pegmatite (T5)

Figure 8

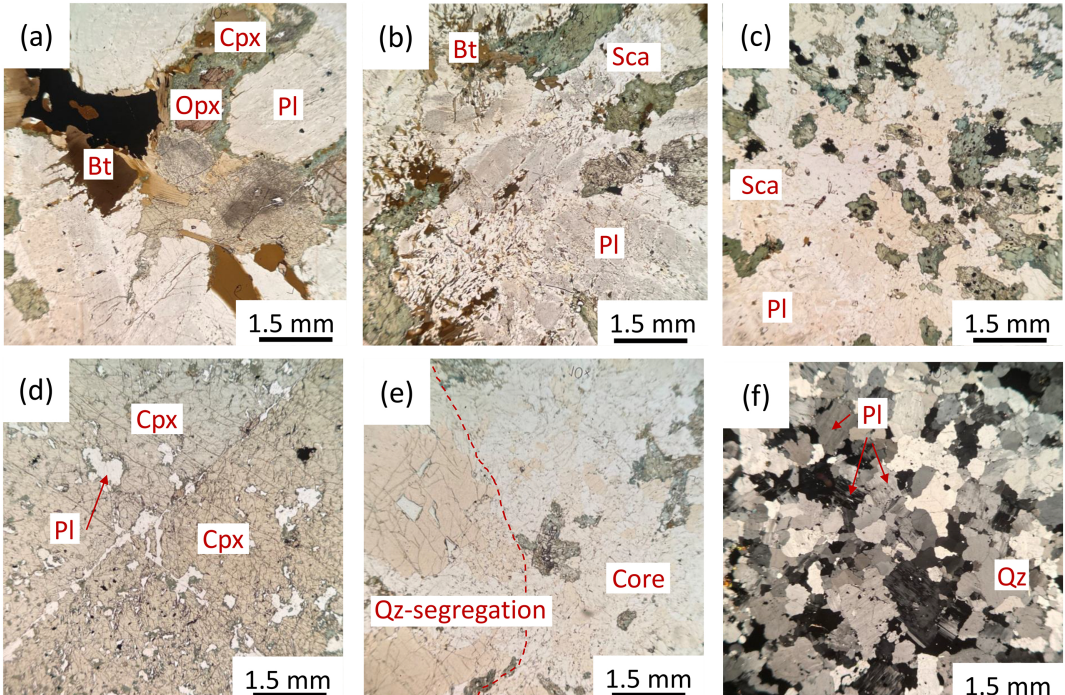
(a)
Cpx
Opx
Pl
Bt
1.5 mm
(b)
Bt
Sca
Pl
1.5 mm
(c)
Sca
Pl
1.5 mm
(d)
Cpx
Pl
Cpx
1.5 mm
(e)
Core
Qz-segregation
1.5 mm
(f)
Pl
Qz
1.5 mm

Figure 9

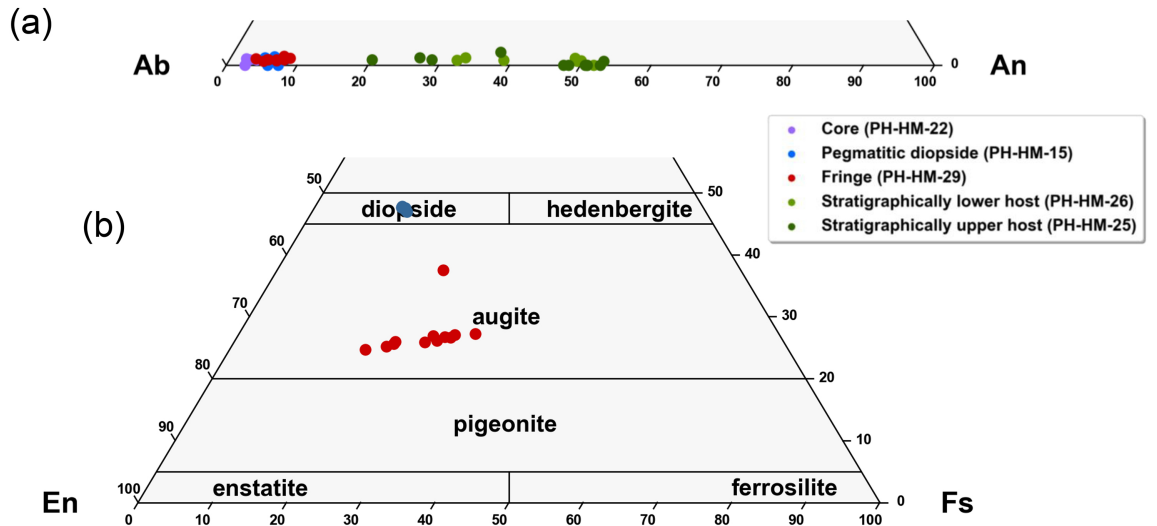
(a)
Ab
An
0
10
20
30
40
50
60
70
80
90
100
0
(b)
Core (PH-HM-22)
Pegmatitic diopside (PH-HM-15)
Fringe (PH-HM-29)
Stratigraphically lower host (PH-HM-26)
Stratigraphically upper host (PH-HM-25)
diopside
hedenbergite
augite
pigeonite
enstatite
ferrosilite
En
Fs
50
60
70
80
90
100
40
30
20
10

Figure 10

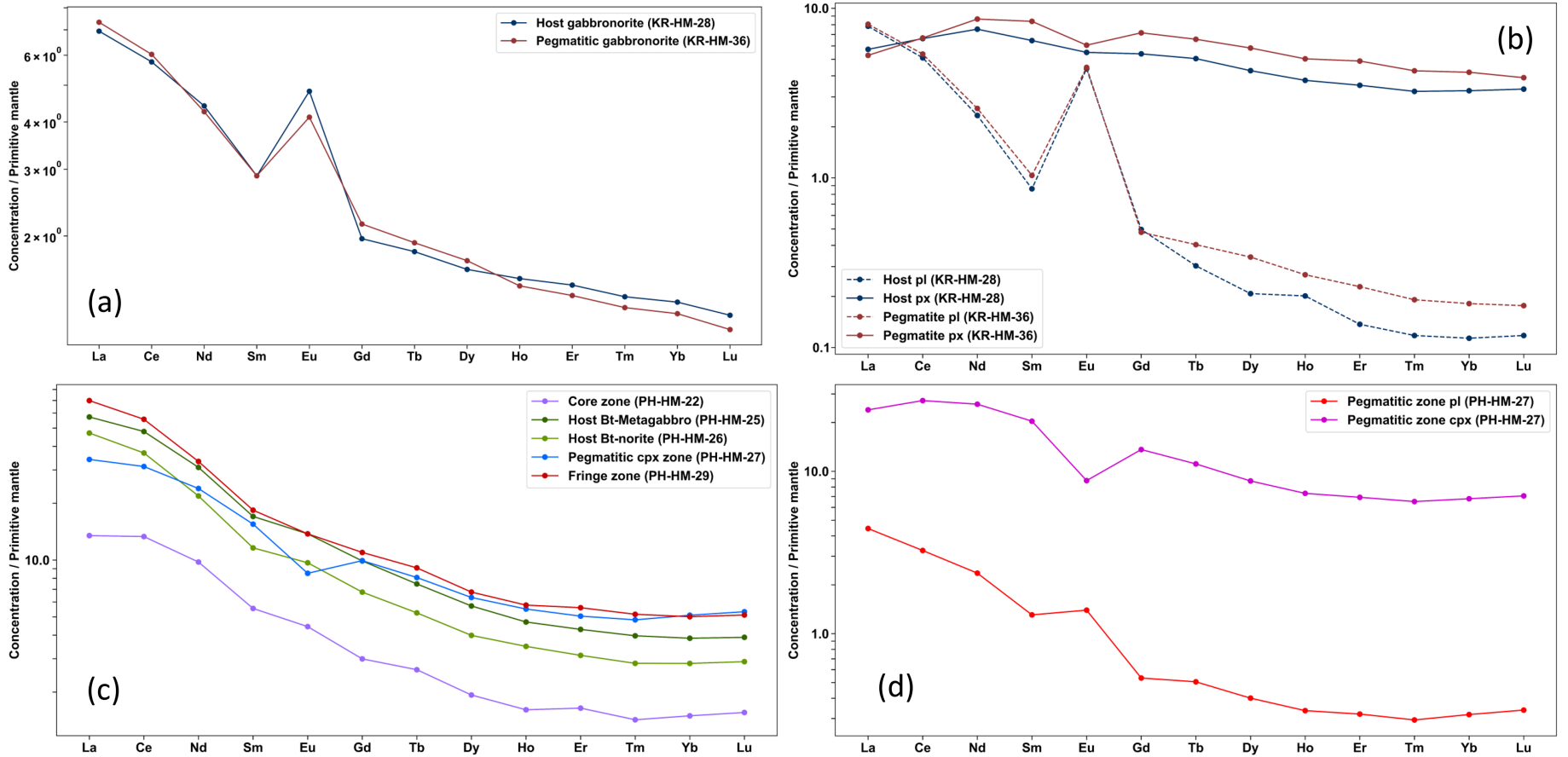
Host gabbronorite (KR-HM-28)
Pegmatitic gabbronorite (KR-HM-36)
Concentration / Primitive mantle
(a)
La Ce Nd Sm Eu Gd Tb Dy Ho Er Tm Yb Lu
(b)
Host pl (KR-HM-28)
Host px (KR-HM-28)
Pegmatite pl (KR-HM-36)
Pegmatite px (KR-HM-36)
(c)
Core zone (PH-HM-22)
Host Bt-Metagabbro (PH-HM-25)
Host Bt-norite (PH-HM-26)
Pegmatitic cpx zone (PH-HM-27)
Fringe zone (PH-HM-29)
(d)
Pegmatitic zone pl (PH-HM-27)
Pegmatitic zone cpx (PH-HM-27)

Figure 11

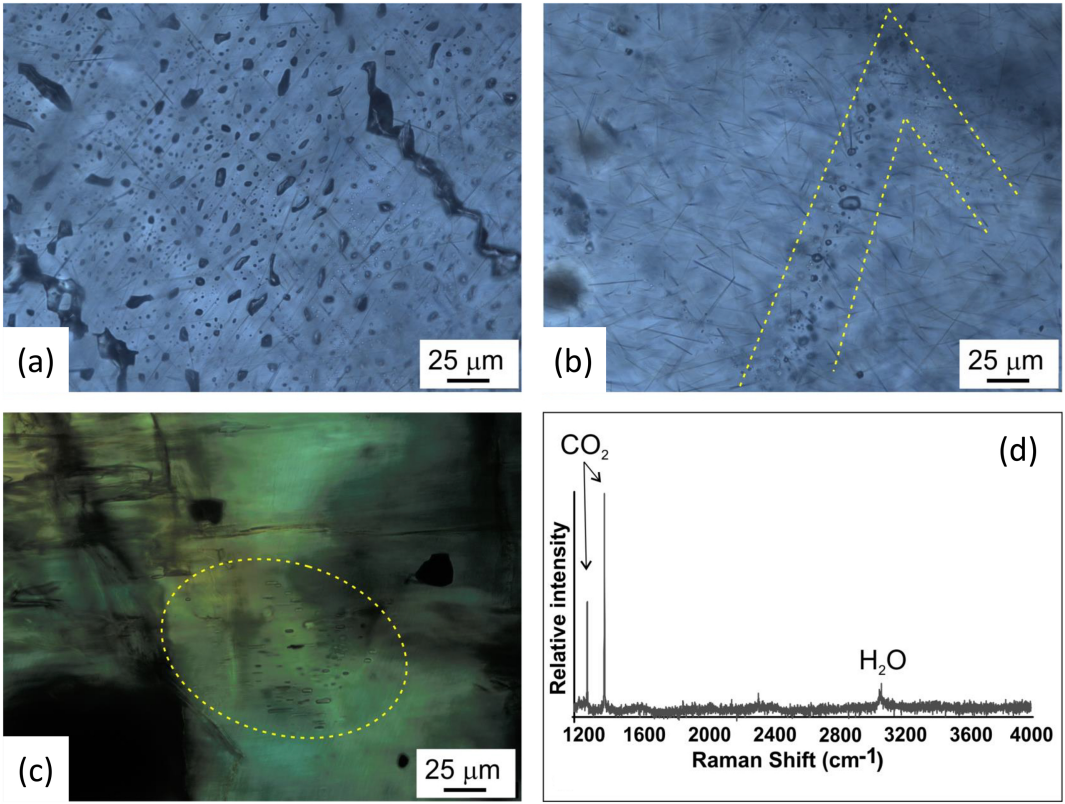
(a)
25 μm
(b)
25 μm
(c)
25 μm
(d)
CO2
H2O
Relative intensity
1200
1600
2000
2400
2800
3200
3600
4000
Raman Shift (cm-1)

Figure 12

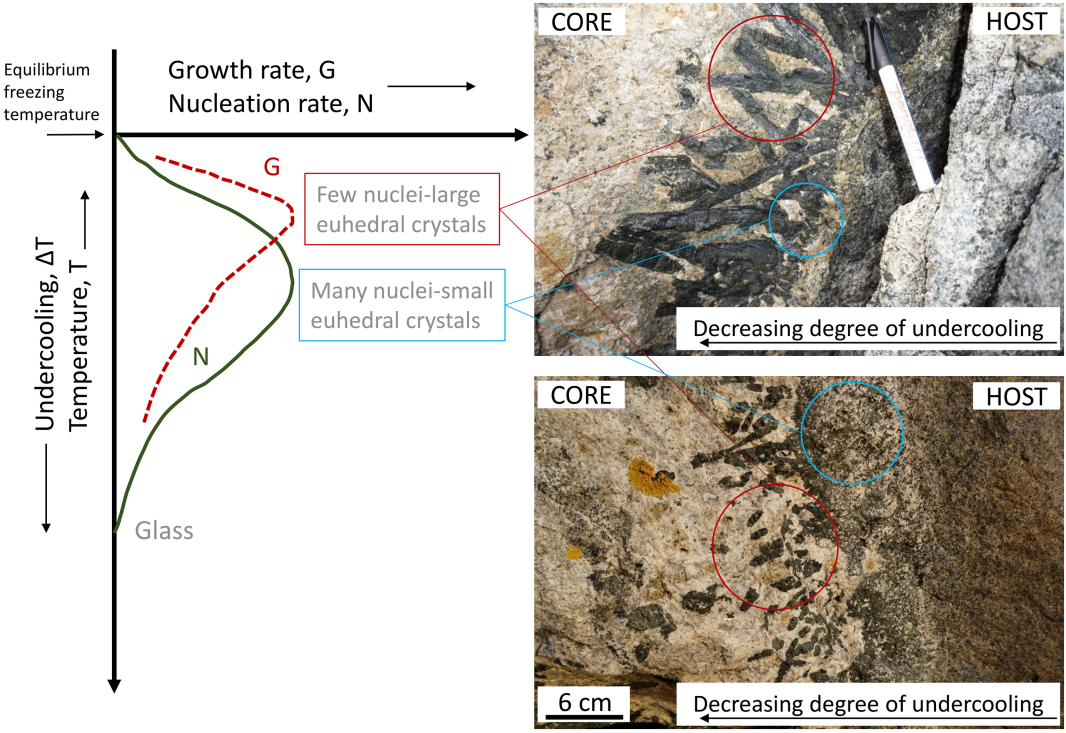
Equilibrium freezing temperature
Growth rate, G
Nucleation rate, N
G
N
Undercooling, ΔT
Temperature, T
Glass
Few nuclei-large euhedral crystals
Many nuclei-small euhedral crystals
CORE
HOST
Decreasing degree of undercooling
CORE
HOST
6 cm
Decreasing degree of undercooling

Figure 13